 VoR: https://doi.org/10.1016/j.geoderma.2017.12.030

RESOLVING COMPACTNESS INDEX OF PORES AND SOLID PHASE ELEMENTS IN SANDY AND SILT LOAMY SOILS

Maja Bryk

Institute of Soil Science, Environment Engineering and Management, University of Life Sciences in Lublin, Leszczyńskiego 7, 20-069 Lublin, Poland

maja.bryk@up.lublin.pl, majabryk@post.pl, phone +48 81 5248148

Abstract

Soil structure is expressed by the size, shape, and arrangement of structural elements. Shape indices of pores and solid phase elements along with the physical soil parameters allow for thorough evaluation of soil structure. Therefore, the aim of the research was the analysis of properties of an index of shape – a compactness index $CMP = (16 \cdot area)/perimeter^2$ – of pore ("pore c-s") and solid phase element cross-sections ("solid c-s") ≥ 100 pix^2 (0.045 mm^2) of 4 soils. *CMP* was calculated via image analysis of resin-impregnated soil blocks prepared from intact soil specimens. The morphometric parameters of the objects assigned to selected *CMP* classes (≤ 0.2, the lowest compactness; 0.201–0.4; 0.401–0.6; 0.601–0.8; 0.801–1; 1.001–1.2; > 1.2, the highest compactness) were compared via 2-way ANOVA for two horizons (A, C) and two textures (sand, silt loam). The usability of *CMP* in the description of soil structure was then tested. Moreover, the relations of the morphometric parameters of the objects in *CMP* classes and soil physical and chemical properties (total organic carbon *TOC*; bulk and particle density; texture; field water capacity *FWC*; field air capacity *FAC*; available water capacity *AWC*; air permeability at –15 kPa lg*FAP*; saturated hydraulic conductivity lgK_S) were examined by way of single and multiple linear regressions. For pore and solid c-s of *CMP* > 0.2 their number, area, and average areas in *CMP* classes decreased with increasing

CMP value. The distributions of pore and solid c-s among *CMP* classes depended on soil texture and structure (aggregate, non-aggregate), allowing for the diagnosis of soil structure status and change. Number and area of objects in *CMP* classes showed numerous strong relations ($R^2 > 0.7$) to the soil physical and chemical parameters for the studied soil textures and horizons. The relations differed for pore and solid c-s and depended also on the object shape (spread, compact or very compact). The average areas of the compact and very compact pore and solid c-s increased with the increase of clay and silt content and the decrease of sand content. The number of pore c-s of *CMP* > 0.2 was related to the texture or particle density. On the other hand, the number of solid c-s of *CMP* > 0.2, and the average area of the most spread solid c-s were related to *TOC* and bulk density. *FWC* and *AWC* increased with the decrease of the number of mainly compact and very compact pore c-s by the decrease of the average area of the most spread solid c-s. Both water capacities increased with the increasing average areas of pore c-s of *CMP* > 0.2 and the average areas of the compact and very compact solid c-s. *FAC* increased with the increase of the number of the compact and very compact pore c-s. lgK_S increased with the increase of the number and area of mostly compact and very compact pore c-s. lg*FAP* increased with the area and the average area of the majority of pore classes and some of the relations were also controlled by the number of pore c-s and the average area of the most spread solid c-s. The study showed moreover that *CMP* increased with the decreasing size of the objects when measured via computer-aided image analysis. Small cross-sections revealed usually larger *CMP* values, and large cross-sections were more often classified as irregular or spread. Therefore the analysis of shape of soil structural elements should encompass a wide range of element sizes in relation to the image resolution to obtain the unbiased shape distributions.

Keywords: Soil structure; Aggregate; Pore; Shape; Compactness index; Soil physical

properties

1. Introduction

Soil structure is defined as the physical constitution of soil material: the solid particles and the voids. Included are both the primary particles forming compound particles, and the compound particles themselves (Canarache et al., 2006). Soil structure is expressed by the size, shape, and arrangement of structural elements. These geometric parameters of soil structure, along with the physical soil parameters related to the soil structure status (bulk density, porosity, air and water permeability, etc.), should be taken into account for thorough evaluation of soil structure. The shape and orientation of soil pores and solid phase elements allows for diagnosis of soil structure change upon external factors (Skvortsova, 2009; Skvortsova and Utkaeva, 2008).

The use of shape indices in the analysis of soil structure has a long history. The initial source of information on the soil structure, allowing for its morphological and morphometric analysis, were 2D images derived on the basis of resin-impregnated thin sections or soil blocks. Most indices developed for 2D analog or digital photographs of structure utilized the area (*area*) and perimeter (*per*) of the pore or solid phase element cross-section. Beckmann (1962) applied "Lappungsquotient" calculated as $per/(4\pi \cdot area)^{0.5}$; Pardini et al. (1996) – index calculated as $area/per^2$; Bouma et al. (1977), Grevers and de Jong (1992), Puentes et al. (1992), Holden (1993), Sakai et al. (1996), Chun et al. (2008) – a roundness (or compactness) index calculated as $4\pi \cdot area/per^2$; Droogers et al. (1998) – "shape" = $per/(4\pi \cdot area)^{0.5}$ and "convex shape" = $(convex\ per)/(4\pi \cdot area)^{0.5}$; Panini et al. (1997), Pérès et al. (1998), Beaudet-Vidal et al. (1998), Hallaire et al. (2000), Pagliai et al. (2004) used an index which equalled $per^2/(4\pi \cdot area)$, referred to as shape or lengthening or elongation index. Skvortsova and

Morozov (1993) and Skvortsova and Sanzharova (2007), in the form factor $F = (4\pi \cdot area/per^2 + W/L)/2$, incorporated also the longer (L) and shorter (W) axes of a minimal rectangle bounding a pore cross-section. New possibilities for soil structure studies emerged in the 1980s when the methods of high-resolution X-ray tomography, commonly called micro-CT, developed rapidly allowing for 3D recognition of numerous soil properties (Cnudde and Boone, 2013; Gerke et al., 2012). In consequence, shape indices for the evaluation of the 3D voids and particles were proposed (e.g. Garbout et al., 2013; Zhou et al., 2012). Although generally applied for 3D visualization and analysis, the micro-CT technique could also produce 2D soil images resembling those of thin sections (e.g. Gerke et al., 2012; Skvortsova et al., 2016). 2D data were also generated by throat-finding algorithms that locate planar cross-sectional areas in the void network to evaluate the drainage process in porous media (e.g. Lindquist, 2006). In both cases the above mentioned shape indices originally developed to study 2D images could still be employed.

The choice of the most appropriate indices describing geometrical properties of soil structural elements depends primarily on the purpose of the research (Droogers et al., 1998). In the classification of soil pore or aggregate cross-sections in the 2D images, probably the most widely used is the circularity (roundness, compactness) index expressed in the general form $b \cdot area/per^2$ (where b usually equals 1 or 4π). The "shape factor" $G = area/per^2$ (Mason and Morrow, 1991; Øren et al., 1998), along with the equivalent roundness (compaction) index $4\pi \cdot area/per^2$ which is the conventional shape factor G normalized by 4π, are applied also in pore-network models which describe flow and transport mechanisms and are used in predicting flow properties of different porous media. The shape factor G and its analogues are important in pore-network models for accurate prediction of fluid volumes and wetting layer conductivities in one- and multi-phase flow and are used to assign the shape of pores and throats during flow simulations (Helland et al., 2008; Miao et al., 2017), because the

dimensionless shape factor *G* shows a strong and monotonic relationship with the dimensionless conductance (e.g. Miao et. al., 2017; Patzek and Silin, 2001; Sholokhova et al., 2009).

The parameters describing the shape of soil pores or solid phase elements are morphological indices which do not have their direct physical analogues. At the same time, the numerical shape indices of soil structural elements are of the major diagnostic value and they support the quantitative evaluation of soil structure status (Skvortsova and Utkaeva, 2008). Consequently, they are widely used. However, even in the recent literature dealing with soil structure studies via computer image analysis, important information about conditions of the shape analysis (number of pixels in the minimal object, method of perimeter calculation, image resolution per pixel, etc.) is neglected rendering the presented results hardly usable. In addition, a systematic knowledge of the shape indices is lacking which hinders the correct interpretation of the shape analysis, since the main attention is paid to the object (soil, geological material, etc.) characterized with the use of shape indices rather than a shape index itself.

Therefore, the aim of the research was the analysis of properties of an index of shape – a compactness index analogous to the above mentioned shape factor *G* – in order to 1) draw attention to its specific characteristics resulting from its measurement via digital images of soil structure, and 2) test its usability in the description of soil structure and soil water and air properties. The compactness index was calculated as $CMP = 16 \cdot area/per^2$, which reflected the shape of cross-sections of soil pore or solid phase element relative to a square, to account for the fact that soil structure was studied via scanned raster images consisting of square pixels. The compactness index was employed in the study, because it was among the most popular indices, i.e. the ones of the "$b \cdot area/per^2$" type, which were commonly used both in the soil structure studies and for the evaluation of hydraulic properties of porous media. The index

was calculated via image analysis of resin-impregnated soil blocks prepared from intact soil specimens taken from 4 soils. Then, the morphometric parameters of the objects in the selected compactness index classes were compared for two horizons (A, C) and two textures (sand, silt loam). Moreover, the relations of the morphometric parameters of the objects in the compactness index classes and soil physical and chemical properties were examined.

2. Materials and methods

2.1. Study site

Soil samples were taken from: Albic Podzol (PZ-ab), Dystric Brunic Arenosol (AR-br.dy), Haplic Chernozem (CH-ha), and Eutric Cambisol (CM-eu) (IUSS Working Group WRB, 2015) located in a possibly slightly changed forest areas of south-eastern Poland. Albic Podzol developed from eolian sand and Dystric Brunic Arenosol – from glacio-fluvial sand, while Haplic Chernozem and Eutric Cambisol developed from loess (Tab. 1).

2.2. Sampling and analysis methods

For the study, A and C or Ck horizons were chosen since they show contrasting chemical and physical properties. The upper A horizons were influenced by a variety of external factors. On the other hand, C horizons were little affected by pedogenetic processes, so they represented a suitable point of reference in the research. From the chosen layers of the soils' A, C or Ck horizons (Tab. 2), samples with preserved structure were taken in 2 replicates in the vertical plane into metal boxes measuring 8×9×4 cm. Dried soil samples were impregnated with a resin solution following the method described earlier (Bryk and

Kołodziej, 2014). After hardening each soil sample was cut and polished into 3 ca. 8×9×1 cm slices, 2 with one and 1 with two sides ready for analysis. For each tested layer in total eight soil block faces were thus obtained. Afterwards, the soil block faces were scanned with a flatbed scanner at a constant resolution of 1200×1200 dpi (1 pix^2 = 21.17×21.17 μm^2) with 24-bit colour depth. Finally, each image was ca. 4000×4000 pixels. The areas of the scanned images varied, because for each sample the maximum rectangle was chosen which omitted the uneven edges of soil blocks. On the basis of the soil blocks and their enlarged photos, morphographic and morphological structure analyses of the tested soils were performed. The structure was described using the terminology given by Słowińska-Jurkiewicz et al. (2012) and Aguilar et al. (2017). The scanned images were used also for morphometric analysis. First, the blue channel which was characterized by the best contrast was isolated from the colour images. The obtained images were recorded in 256 shades of grey, with prior improving of their contrast and intensity. Subsequently, on the images a sequence of operations and measurements was made using the image analysis program Aphelion (Adcis SA). First, the images were thresholded, i.e. the limit value of grey level between the solid phase and pores was selected manually based on the brightness histogram and visual evaluation of an enlarged photo of the block, to obtain binary (B&W) images. It was not possible to apply an automatic thresholding due to a very large complexity of the images of the studied soils' structure. The objects, i.e. cross-sections of pores and cross-sections of solid phase elements, were then subjected to measurements. The used scanning resolution limited the minimum diameter of the measured object to 21.17 μm – the size characteristic to macropores. Nevertheless, the measurements described below were done only for objects ≥ 100 pix^2 (0.045 mm^2) because the results were used for retrieving a compactness index – which is one of shape indices – and the shape of objects smaller than 100 pix^2 in a square grid of pixels in an image could not be sufficiently resolved. The 100 pix^2 area corresponded to a

circle of an equivalent diameter of 239 μm. Utilizing the data from the entire extent of each image the areas of pore and solid phase element cross-sections, A_{Pi} and A_{Si} (pix^2), were measured by counting the number of pixels in each object. The number (N_P, N_S) and perimeters (L_{Pi}, L_{Si}; pix) of pore and solid phase element cross-sections were, on the other hand, determined for the cross-sections which centroids were located within a protective frame to avoid a statistical bias of the counting of the objects. In general, with a protective-frame procedure the objects crossing the edges of the frame and the ones in the corners are properly counted one time, instead of, respectively, 2 or 4 times when adjacent frames are analysed during the image analysis (Wojnar et al., 2002). The applied protective frame was smaller than the scanned image and included the centrally-placed rectangular covering 90.25% of the area of each image, i.e. 95% × width × 95% × height of the image. The perimeters were measured in Aphelion program with the use of the Crofton formula, $L_i = (\pi/4)[N_0 + N_{90} + (\sqrt{2}/2)(N_{45} + N_{135})]$, where L_i is a normalized count of the number (N_0, N_{45}, N_{90}, N_{135}) of occurrences of 0, 45 90, and 135 degree edges in each object (ADCIS SA, AAI Inc., 2010). The obtained tables with measurements for each soil block were then processed in a spreadsheet. Before subsequent calculations, the values in pixels were converted into physical units knowing that 1 pixel had the size of 21.17 μm × 21.17 μm.

In the studied genetic horizons of each soil total area of pore and solid phase element cross-sections ($A_P = \Sigma A_{Pi}$ and $A_S = \Sigma A_{Si}$; mm^2) were evaluated. Then the relative area, $A_{AP} = A_P/A$ and $A_{AS} = A_S/A$ (cm^2 dm^{-2}), and the relative number of pore and solid phase element cross-sections, $N_{AP} = N_P/A_R$ and $N_{AS} = N_S/A_R$ (dm^{-2}) were calculated. A and A_R were the total area of the image and the area of the protective frame, respectively, and later in the paper they will be referred to as the sample area. Next, a compactness index for each pore and solid phase element cross-section was calculated: $CMP_{Pi} = 16A_{Pi}/L_{Pi}^2$ and $CMP_{Si} = 16A_{Si}/L_{Si}^2$, respectively (ADCIS SA, AAI Inc., 2010). The whole range of *CMP* values was divided into

7 classes: 0.000–0.200 (k = 1), 0.201–0.400 (k = 2), 0.401–0.600 (k = 3), 0.601–0.800 (k = 4), 0.801–1.000 (k = 5), 1.001–1.200 (k = 6), and > 1.200 (k = 7). It allowed to study the distributions of pore or solid phase element cross-sections among *CMP* classes and to observe the objects' properties in these classes without the need of prior assignment of *CMP* values to specific shapes. Afterwards the number (N_{Pk} and N_{Sk}) and sum of area (A_{Pk} and A_{Sk}) of pore or solid phase element cross-sections in the selected classes of compactness index were calculated and related to the sample area: $N_{APk} = N_{Pk}/A_R$, $N_{ASk} = N_{Sk}/A_R$ (dm^{-2}), and $A_{APk} = A_{Pk}/A$, $A_{ASk} = A_{Sk}/A$ (cm^2 dm^{-2}). The average area of a pore or a solid phase element cross-section in compactness index classes was calculated as: $AN_{Pk} = A_{Pk}/N_{Pk}$ and $AN_{Sk} = A_{Sk}/N_{Sk}$ (mm^2).

The samples representing genetic horizons A, C or Ck (Tab. 2) for the measurement of the selected soil properties were taken from the same depths as the samples for the evaluation of soil structure. Bulk 1-kg samples with disturbed structure were utilized to determine soil texture (c_s, sand 0.05–2 mm; c_{si}, silt 0.002–0.05 mm; and c_c, clay <0.002 mm fraction content, g g^{-1}, by a combination of the hydrometer and the wet-sieve methods; Polish Society of Soil Science, 2009), total organic carbon (*TOC*, mg g^{-1}; PN-ISO 14235, 2003), carbonates ($CaCO_3$, mg g^{-1}, by the volumetric Scheibler method; PN-ISO 10693, 2002), and particle density (ρ_s, g cm^{-3}, by the pycnometer method; PN-ISO 11508, 2001). Moreover, in 12 replicates, soil samples with preserved structure were taken vertically into metal cylinders with a volume of 100 cm^3. Six of them were applied to determine the dry soil bulk density (ρ_d, g cm^{-3}) by the thermogravimetric method and soil moisture at soil water potentials 0 kPa (maximum water capacity, *MWC*, cm^3 cm^{-3}), –15 kPa (field water capacity for a soil with a deep groundwater table, *FWC*, cm^3 cm^{-3}), and –1550 kPa (permanent wilting point, *PWP*, cm^3 cm^{-3}) balanced in pressure chambers on ceramic plates. At the potential –15 kPa, air permeability (*FAP*, field air permeability, $10^{-8} \times$ m^2 Pa^{-1} s^{-1}) was also measured in the device

designed to test the permeability of moulding sands, LPiR-2e (Multiserw-Morek, Poland). The measurement was carried out at the constant ambient temperature (20±0.5°C), therefore the dynamic viscosity of air did not require consideration. In the additional 6 samples collected in the corresponding cylinders, saturated hydraulic conductivity (K_S, cm h^{-1}) was measured by a constant head method using the ICW laboratory permeameter (Eijkelkamp, The Netherlands). Total porosity of the soil (P_O, cm^3 cm^{-3}) was calculated on the basis of the soil bulk and soil particle density. Field air capacity (*FAC*, cm^3 cm^{-3}) was calculated as the difference between maximum water content and field water capacity, $FAC = MWC - FWC$. Available water capacity (*AWC*, cm^3 cm^{-3}) was calculated as $AWC = FWC - PWP$.

2.3. Statistical analyses

The measured variables were tested for normality of variance using the Kolmogorov-Smirnov test. The field air permeability (*FAP*) and the saturated hydraulic conductivity (K_S) were not normally distributed, thus data were log-transformed prior to statistical analyses. Next, two-way analysis of variance (ANOVA) was used to compare measured parameters for horizons (A, C or Ck) and textures (sand, silt loam) ($P < 0.05$). Subsequently Tukey's honestly significant difference test was performed at $P < 0.05$. The single and multiple linear regressions (n=8) were calculated to search for relations between the morphometric parameters' values and the selected physical and chemical soil properties.

3. Results

3.1. Physicochemical properties

Table 2, 3, and S1 show selected physical and chemical properties of the studied soils. Podzol and Arenosol were characterized by a sandy texture, while Chernozem and Cambisol were silt loamy. The carbonates were detected in Ck horizons of Haplic Chernozem and Eutric Cambisol, in the amount of 104 and 110 mg g^{-1}, respectively. On average, sandy soils were characterized with higher sand fraction and lower silt and clay fraction content, and showed higher bulk density and lower particle density than the silt loamy soils (Tab. 3). Furthermore, as expected, A horizons revealed higher *TOC*, lower bulk and particle density than C or Ck horizons and, consequently, higher total porosity. Moreover, the studied soils showed typical water and air properties which arose from the observed soil textures and chemical properties, and a structure characteristic for forest soils without anthropogenic impact. Maximum water capacity (*MWC*) was higher in A horizons and in silt loamy soils. Field water capacity (*FWC*), field air capacity (*FAC*), and permanent wilting point (*PWP*) depended on soil horizon and texture. *FWC* was the highest and the *FAC* the lowest in Ck horizons of silt loamy soils, and the opposite values were detected in C horizons of sandy soils. The A horizons of both textures were characterized with intermediate values of both *FWC* and *FAC*. *PWP* was the lowest in C horizons of sandy soils. Available water capacity (*AWC*) was higher for silt loamy soils. Field air permeability (*FAP*) and hydraulic conductivity (K_S) followed generally the similar pattern, i.e. these parameters were the lowest in Ck horizons of silt loamy soils and higher for other samples.

3.2. Soil structure

In the Albic Podzol (PZ-ab) the PZ-ab2 layer, representing A horizon, was penetrated by roots (Fig. 1, a). Sand grains were joined by bridges of dark humic colloids. In the soil groundmass there were also visible numerous intergrain channels of almost circular cross-

sections created by roots (Fig. 1, b) and also very large channels of round or oval shapes up to 25 mm in diameter made by soil fauna (Fig. 1, c). In the PZ-ab7 layer (C horizon of parent material) next to the zones of structure with single grains and compact grains (Fig. 1, d) there were also numerous planes forming the zones of the structure with weakly-developed sub-angular blocks (Fig. 1, e).

The soil groundmass of the AR-br.dy2 layer from A horizon of the Dystric Brunic Arenosol (AR-br.dy) was characterized by a non-aggregate structure with sand grains bridged by humic colloids (Fig. 1). In the mineral groundmass there were visible biogenic channels up to 15 mm in diameter; some of them contained roots (Fig. 1, f). The roots were most abundant in the upper layer of the A horizon. The AR-br.dy5 layer of the parent material had a non-aggregate structure with simple packing voids and small vughs (Fig. 1, g).

In the Haplic Chernozem (CH-ha), soil fauna activity was extensive and bioturbations were one of the most important processes shaping the whole pedon. The CH-ha1 layer, representing the A horizon, was penetrated by plant roots and showed the presence of numerous channels – krotovinas made by abundant soil fauna (Fig. 1). CH-ha1 layer revealed an aggregate structure with crumbs developed to varying degrees (Fig. 1, h). Biogenic channels and chambers with smooth walls were the dominant pores (Fig. 1, i). In the zones of weakly-developed aggregates the soil groundmass was more compacted, with the pores – planes (Fig. 1, k). Between planes and channels, small vughs – *Nadelstichporen* – were visible. The Ck horizon (CH-ha5) was loess of a non-aggregate structure, with slight changes due to bioturbations (Fig. 1, l), and pores in the form of vughs (Fig. 1, m).

The CM-eu2 layer representing A horizon of the Eutric Cambisol (CM-eu), was vastly penetrated by tree and shrub roots, and has mostly an aggregate structure (Fig. 1). Crumbs (Fig. 1, n) were arranged quite tightly and sub-angular blocks were separated by planes (Fig. 1, o). In the lower part of the layer the were visible more compacted zones characterized by a

non-aggregate structure with biogenic channels and small vughs (*Nadelstichporen*) (Fig. 1, p). The CM-eu7 layer, representing parent material – a calcareous loess (Ck), had mostly non-aggregate structure, with characteristic of loess tiny vughs (Fig. 1, r). The traces of soil fauna activity were less evident, nevertheless some areas could be found where the bioturbations were visible with both the 10-mm-wide earthworm channels (Fig. 1, s) and zones strongly fragmented by animals.

3.3. Morphometric parameters in the compactness index classes

The applied compactness index (*CMP*) was a description that expressed the shape of an object relative to a square and reflected variations in the gross shape of an object. The *CMP* was analogous to the previously mentioned shape factor $G = area/per^2$, or roundness (or compactness) index calculated as $4\pi \cdot area/per^2$ for which, however, the reference figure was a circle instead of a square. In the current paper as a reference a square was chosen, because it could be equally reproduced in the 2D Euclidean space and, when oriented along the X and Y axes, in the grid of discrete square pixels which constitute an image of soil structure. The shapes other than rectangular, e.g. circles, cannot be faithfully represented in raster computer images. This faithful representation of the reference figure was obviously not necessary for proper calculations, but was intended to provide some conceptual coherence between a discrete representation of soil structure via digital images and a continuous geometry from which mathematical methods for evaluation of shape indices were derived. The compactness index was thus calculated as $CMP = 16A/L^2$ with perimeter, L, estimated via the Crofton formula. This formula gives a more accurate estimate of an object's Euclidean perimeter than the methods based on the counting of number of pixels along the object's boundary and is also less sensitive to the object's orientation. Consequently, *CMP* values were confined in a

theoretical range from 0 to $4/\pi$; it had values close to 0 for branched or long and thin shapes, reached 1 for a square and $4/\pi = 1.27$ for a circle (Fig. 2). The distributions of pore or solid phase element cross-sections among selected *CMP* classes: 0–0.2 ($k = 1$), 0.201–0.4 ($k = 2$), 0.401–0.6 ($k = 3$), 0.601–0.8 ($k = 4$), 0.801–1 ($k = 5$), 1.001–1.2 ($k = 6$), and > 1.2 ($k = 7$), were then studied.

Total relative number of pore cross-sections > 100 pix^2 N_{AP} (dm^{-2}) was higher for sandy soils (Tab. 4 and S2). It was due to the fact that sandy soils were characterized mostly with separate (discrete) inter-grain pores. In silt loamy soils larger, and, consequently, less numerous inter-aggregate pores developed. Humic A horizons of the studied soils, regardless of their texture, revealed higher relative number of pore cross-sections. For *CMP* ≤ 0.2 and 0.401–1, the relative number of pore cross-sections depended on soil texture and horizon. The lowest N_{APk} were generally detected in C or Ck horizons of silt loamy soils, intermediate in the A horizons of silt loamy soils, and the highest in both studied horizons of sandy soils. The N_{AP2} values (*CMP* 0.201–0.4) were on average higher for sandy than for silt loamy soils, and for A than for C or Ck horizons. These trends detected for *CMP* ≤ 1 mimicked in general the situation observed for the total relative number of pore cross-sections N_{AP}. The most compact pore cross-sections of *CMP* > 1 were, in contrast, more abundant in silt loamy than in sandy soils and also more abundant in C or Ck than in A horizons. For all the studied soils the unimodal distribution of the number of pore cross-sections among the compactness index classes was detected (Fig. 3a) and the highest N_{APk} values were observed for *CMP* 0.201–0.6. Moreover, it was observed for the two studied soil textures that in the A horizons of silt loamy soils there was a lower fraction of pore cross-sections of *CMP* 0.201–0.4 and higher – pores of *CMP* > 0.8 than in sandy soils. The Ck horizons of silt loamy soils showed higher fraction of pore cross-sections with *CMP* ≤ 0.2 and *CMP* > 0.8 but lower with *CMP* 0.201–0.6 than C horizons of sandy soils. The distributions in each texture group depended also on soil horizon

(Fig. 3a). In sandy soils the fraction of pore cross-sections with *CMP* ≤ 0.4 was lower and with *CMP* > 0.4 higher in A horizons in comparison with C horizons. In silt loamy soils the fraction of pores with *CMP* 0.201–0.6 was higher and with *CMP* > 0.8 lower in A horizons than in Ck horizons.

Total relative area of pore cross-sections > 100 pix^2 A_{AP} (cm^2 dm^{-2}) in A horizons was higher for silt loamy soils but in C or Ck horizons these values were very similar (Tab. 4). The relative area values for pores of *CMP* ≤ 0.2 and 0.401–1 varied depending on soil texture and horizon. A_{AP1} was the highest in A horizon of silt loamy soils and lower and similar in A horizons of sandy soils and C or Ck horizons of all soils regardless of their texture. Smaller differences were observed for A_{AP3}, A_{AP4}, and A_{AP5} values, where the lowest values of these parameters were detected generally in Ck horizons of silt loamy soils. A_{AP2} values were higher for sandy than for silt loamy soils and higher in A horizons in comparison with C or Ck horizons. The area fraction of pores of *CMP* ≤ 0.4 was the largest and in consequence the area distributions followed a negative exponential function (Fig. 3c), in contrast to number distributions (Fig. 3a), which nearly followed a normal distribution function. In the A horizons of sandy soils there was a lower fraction of pore cross-sections of *CMP* ≤ 0.2 and higher – pores of *CMP* 0.201–1 than in silt loamy soils (Fig. 3c). Similar pattern was observed in C and Ck horizons. Moreover, for both studied soil textures the fraction of area of pore cross-sections with *CMP* ≤ 0.2 decreased and with *CMP* 0.201–1.2 increased in C or Ck horizons in comparison to the relevant A horizons.

The average areas of a pore cross-section in each *CMP* class resulted directly from the measured N_{Pk} and A_{Pk} values (Tab. 4). The number of pore cross-sections of *CMP* ≤ 0.2 was relatively low and they occupied large area, consequently the average area of a pore cross-section AN_{P1} exceeded noticeably the average areas of pore cross-section of *CMP* > 0.2. The highest average area had the pore cross-sections of *CMP* ≤ 0.2 in A horizons of silt loamy

soils and the value of this parameter was similar for other soils and horizons. For *CMP* > 0.2, AN_{P2}–AN_{P7} values were similar in both studied horizons and were higher in silt loamy soils (Tab. 4, Fig. 4a). For *CMP* > 0.4 the average areas of a pore cross-section were limited to quite narrow ranges: 0.041–0.085 and 0.070–0.121 for sandy and silt loamy soils, respectively. As for *CMP* > 0.2 the N_{APk} and A_{APk} values decreased simultaneously, a close linear regression between the log values of both parameters was detected (Fig. 4a).

CMP_{Pi} values decreased with the increase of pore cross-sectional area, A_{Pi} (Fig. 5), following the general function $\lg CMP_i = -a - b \lg A_i - c \lg A_i^2$ (Tab. S3). For *CMP* ≥ 0.4, A_{Pi} did not exceed, depending on soil texture and horizon, the value of: 13.8 mm^2 (4.2 mm equivalent diameter; CH-ha1), 4.0 mm^2 (2.3 mm; PZ-ab2), 1.6 and 1.2 mm^2 (1.4 and 1.2 mm; AR-br.dy2, PZ-ab7 and CM-eu2, CM-eu7, CH-ha5, respectively), and 0.5 mm^2 (0.8 mm; AR-br.dy5). These results suggested that higher *CMP* values were characteristic for pores of small cross-sectional areas. The areas of pores of *CMP* > 0.2, and particularly with *CMP* > 0.4, were substantially less varied than the areas of pore cross-sections of *CMP* ≤ 0.2. Both small and very large pores were assigned to the latter class.

The studied soils were characterized by much lower number of solid phase element cross-sections in comparison with the number of pore cross-sections (Tab. 5 and S4). Both for the total relative number of solid phase element cross-sections > 100 pix^2, N_{AS}, and for objects of *CMP* ≤ 1.2, the highest number of cross-sections was detected in A horizons of silt loamy soils (Tab. 5). Sandy soils in A and C horizons and silt loamy soils in Ck horizons were characterized with similar from the statistical point of view relative number of cross-sections. The N_{AS7} value was higher in A horizons regardless of soil texture. The number distributions of solid phase element cross-sections among *CMP* classes were unimodal with a maximum for *CMP* 0.401–0.6 for A horizons, *CMP* 0.201–0.4 for Ck horizons of silt loamy soils, and *CMP* 0.601–0.8 for C horizons of sandy soils (Fig. 3b). The silt loamy soils revealed in A

horizons higher fraction of solid phase element cross-sections with $CMP \leq 0.2$ and lower with $CMP > 0.2$ in comparison with sandy soils. The distribution in C and Ck horizons depended strongly on soil texture. Sandy soils had lower fraction of solid phase elements with $CMP \leq 0.6$ and higher with $CMP > 0.6$ than silt loamy soils. The distributions of the measured objects among *CMP* classes in each texture group depended also on soil horizon. In silt loamy soils they were virtually identical for both studied horizons. Sandy soils, on the contrary, showed higher fraction of solid phase element cross-sections with *CMP* 0.201–0.6 and lower with $CMP > 0.8$ in A horizons than in C horizons.

The total relative area of solid phase element cross-sections > 100 pix^2, A_{AS}, and the analogous value measured for cross-sections of $CMP \leq 0.2$ (A_{AS1}) depended on soil texture and horizon (Tab. 5). These parameters were the highest in C or Ck horizons of sandy and silt loamy soils, intermediate in A horizons of sandy soils, and the lowest in A horizons of silt loamy soils. The distributions of solid phase elements among *CMP* classes were almost identical regardless of soil horizon or texture (Fig. 3d). The largest area (96.7–100 %) was occupied by objects with $CMP \leq 0.2$. In each of the other *CMP* classes not more than 1.6 % of objects were detected.

As the result of the measured N_{ASk} and A_{ASk} values, the highest A_{NSk} values were observed for $CMP \leq 0.2$ (A_{NS1}) (Tab. 5, Fig. 4b). The average area A_{NS1} depended on soil horizon and texture and was generally lower in silt loamy soils and in A horizons. For cross-sections of $CMP > 0.2$ the average areas of a solid phase element cross-section were 2–3 orders of magnitude lower than for $CMP \leq 0.2$, and decreased gradually. For *CMP* 0.201–1 the average areas of a solid phase cross-section were higher in silt loamy soils. Moreover, for solid phase elements of *CMP* 0.201–0.4, 0.801–1 and > 1.2 this parameter was higher in A horizons, and for *CMP* 0.401–0.8 and 1.001–1.2 it did not depend on soil horizon. A_{NS6} values were uniform regardless of soil horizon and texture.

Similarly as for pores, CMP_{Si} values decreased with increasing area of solid phase element cross-section A_{Si} (Fig. 6). For $CMP \geq 0.4$, depending on soil horizon and texture, A_{Si} was not higher than 6.4–7.9 mm^2 (2.9–3.2 mm equivalent diameter; CM-eu1, AR-br.dy2, PZ-ab2, and CH-ha1), 4.6 and 5.6 mm^2 (2.4 and 2.7 mm; CM-eu7 and CH-ha5, respectively), and 0.2 and 0.3 mm^2 (0.5 and 0.6 mm; AR-br.dy5 and PZ-ab7, respectively).

3.4. Relations of morphometric parameters in compactness index classes with soil chemical and physical properties

The relations of morphometric parameters for pores and solid phase elements with selected physical and chemical properties were studied via single and multiple linear regression analysis (Tab. 6). Total relative area of pore cross-sections > 100 pix^2 A_{AP} (cm^2 dm^{-2}) and the relative area of pore cross-sections of $CMP \leq 0.2$ (A_{AP1}) increased with increasing *TOC* and decreasing ρ_d. The relative area of pore cross-sections of *CMP* 0.201–0.4 (A_{AP2}) depended strongly on both *TOC* and ρ_s. The relative area of pores of *CMP* 1.001–1.2 (A_{AP6}) was strongly linked with ρ_s and the texture – specifically with the content of clay fraction, c_c. The relative area of pore cross-sections of *CMP* > 1.2 (A_{AP7}) increased with the increase of clay, c_c, content (Tab. 6).

The relative number of pore cross-sections of the lowest compactness, i.e. of $CMP \leq 0.2$ (N_{AP1}) was associated with *TOC* and ρ_s, and the relative number of pores of *CMP* 1.001–1.2 (N_{AP6}) depended on ρ_s. Moreover, it was stated that both the total relative number of pore cross-sections (N_{AP}) and relative number of pore cross-sections of *CMP* 0.201–0.4 (N_{AP2}) were closely related to the soil texture (content of sand or silt fraction) and soil particle density. The relative numbers of other groups of pores of *CMP* 0.401–1 and > 1.2 (N_{AP3}–N_{AP5} and N_{AP7}, respectively) were closely related to the texture (c_s, c_{si}, and c_c) of the studied soils.

Similarly, the average areas of a pore cross-section of *CMP* 0.401–1.2 (AN_{P3}–AN_{P6}) depended on the content of clay fraction (Tab. 6).

Total relative area of solid phase element cross-sections > 100 pix^2 (A_{AS}) and the relative area of objects of *CMP* ≤ 0.2 (A_{AS1}) depended on *TOC* and ρ_d (Tab. 6). Similar, although single, linear regressions were observed for the total relative number (N_{AS}) and the relative numbers of solid phase element cross-sections in the studied *CMP* classes (N_{AS1}–N_{AS7}), when the relative number of objects increased with increasing *TOC* and decreasing ρ_d. The average areas of a solid phase element cross-section of *CMP* 0.401–1.2 (AN_{S3}–AN_{S6}) depended on the soil texture. For the solid phase element cross-sections of *CMP* ≤ 0.2 and > 1.2, however, the average object area (AN_{S1} and AN_{S7}, respectively) was associated with *TOC* and ρ_d or with *TOC* only (Tab. 6).

The relations of water and air properties vs. morphometric parameters in compactness index classes were presented in Table 7. *FWC* and *AWC* increased with increasing average areas of a pore cross-section of *CMP* > 0.2 (AN_{P2}–AN_{P7}) and the average areas of a solid phase element cross-section of *CMP* 0.401–1.2 (AN_{S3}–AN_{S6}). Both water capacities were dependent moreover on the relative number of the selected pore cross-section classes (N_{APk}) and at the same time on the average area of a solid phase element cross-sections of *CMP* ≤ 0.2 (AN_{S1}). Field air capacity, *FAC*, increased with the increase of the total relative number of pore cross-sections (N_{AP}) and relative number of pores of *CMP* 0.401–1.2 (N_{AP3}–N_{AP6}) and the area of pores of *CMP* 0.401–1 (A_{AP3}–A_{AP5}). *FAC* was also influenced by the total relative area of solid phase elements (AN_S) and the relative area of solid phase elements of *CMP* ≤ 0.2 (AN_{S1}).

Field air permeability, expressed as lg*FAP*, revealed single linear regressions with the relative area of pores of *CMP* 0.201–1 (A_{AP2}–A_{AP5}). The value of lg*FAP* increased also with the increase of the average areas of a pore cross-section of *CMP* > 0.4 (AN_{P3}–AN_{P7}). Field air

permeability (lg*FAP*) depended moreover on the average area of a pore cross-section of *CMP* ≤ 0.2 (AN_{P1}) in connection with the relative number of pore cross-sections of *CMP* 0.201–1 (N_{AP2}–N_{AP5}) or the average area of a solid phase element cross-section of *CMP* ≤ 0.2 (AN_{S1}). lg*FAP* depended strongly on the relative area of pore cross-sections of *CMP* ≤ 0.2 (A_{AP1}) and the average area of a solid phase element cross-section of *CMP* ≤ 0.2 (AN_{S1}). The observed relations were only positive, i.e. the value of lg*FAP* increased along with the increasing morphometric parameters.

For the hydraulic conductivity represented by lgK_S several links with the calculated morphometric parameters were found. The value of lgK_S increased with the increase of the relative area of pore cross-sections of *CMP* 0.201–1 (A_{AP2}–A_{AP5}) and the relative number of pore cross-sections of *CMP* 0.401–1 (N_{AP3}–N_{AP5}). The relations were however weaker than the ones detected for the field air permeability (lg*FAP*).

4. Discussion

Shape indices give valuable information about soil structure status. Nevertheless, the application of shape indices requires to consider several issues. Firstly, according to some authors (e.g. Czachor and Lipiec, 2004; Ringrose-Voase, 1996; Vogel et al., 1993), shape indices can be measured only for separate, discrete objects (cross-sections). When the cross-sections join together, the unambiguous evaluation of area, perimeter or diameter is not possible. Soil is, however, a system of two intertwining phases (pores and solid phase elements) that form a certain continuum of arrangements from discrete pores in a continuous solid phase (as for massive structure) to discrete solid phase elements with continuous pores (as for a structure with strongly-developed aggregates) (Bryk, 2008). The correct separation of continuous pores or solid phase visualised by various techniques into isolated objects can

only be done in the 3D images of the porous medium geometry, where the throats – the positions of local minimum cross-sectional area in the pore network – or contact areas of aggregates could be found (e.g. Kim et al., 2013; Peth et al., 2008). In this context, the separation of continuous void or solid phases into discrete objects in the 2D images of soil structure does not seem justified and therefore it has not been done in the current study.

The second problem with the use of shape indices arises when the values of shape index have to be chosen to classify the studied objects. These boundaries are usually more or less arbitrary and depend on the specific use of the shape index. In the current paper the *CMP* values were grouped into 7 classes to study the properties of pore or solid phase element cross-sections in relation to their *CMP* value. In the whole presented range of *CMP* values in practice 3 main groups could be selected with respect to the object shapes observed in the soil structure specimen in the macroscale with unaided eye. Cross-sections (shapes) of $CMP > 0.8$ (assigned to classes 5–7) could be described as "very compact", and that of *CMP* 0.401–0.8 (classes 3 and 4) as "compact" (Fig. 2). The cross-sections of $CMP \leq 0.4$ (classes 1 and 2), in relation to their geometrical characteristics, could be referred to as "spread" or "irregular".

The A horizons of the studied soils were characterized by an accumulation of humified organic matter closely mixed with the mineral fraction and morphology that was different from the C horizon, since in these horizons all or much of the original rock structure had been obliterated. C horizons, by definition, are horizons that are little affected by pedogenetic processes and lack properties of H, O, A, E or B horizons. C and Ck horizons of the studied soils had the non-aggregate structure. At the same time A horizons of sandy soils were characterized with a looser arrangement and A horizons of silt loamy soils had the aggregate structure. These different features of the studied genetic horizons were visible in the soil structure images (Fig. 1) and also in the distribution by number or area of pore and solid phase element cross-sections among *CMP* classes (Fig. 3). The compactness index

distributions depended on soil texture and structure. The *CMP* distributions of pore cross-sections in A horizons of silt loamy soils revealed the larger number of branched and spread shapes in comparison with the Ck horizons. In the Ck horizons an increase of the number of the very compact pores was noted, since in this parent material derived from calcareous loess there were many characteristic small and round pores – *Nadelstichporen*. It was stated for the sandy soils, that the spread solid phase elements were numerous in A horizons and compact ones – in C horizons. The compactness index for pore and solid phase element cross-sections could be thus a sensitive measure of soil structure changes and differences. In practice the number distributions were more legible than the area distributions. The area distributions for solid phase elements were the least useful since the percentage of the most spread cross-sections dominated over other classes which made the distributions for the studied soils and horizons indistinguishable.

Compactness index values decreased with the increase of pore cross-sectional area and higher *CMP* values were generally characteristic for pores of small cross-sectional areas. On the other hand, both small and very large pores were assigned to the class of low *CMP* (≤ 0.2). Similar results were presented by other authors, although a direct comparison of data was not always possible due to the different methods of pore identification and dissimilar pore size ranges. What is more, the size of the minimal analysed object and the method of the perimeter evaluation were rarely provided, although both factors significantly influence the distributions of the shape index values. Pérès et al. (1998) detected for a sandy-loam clay and a loamy clay soil the largest fraction of rounded pores in the class of small pores (with equivalent diameter < 2 mm which corresponded to $\lg A_P$ ca. 0.5). For pores with equivalent diameter > 2 mm, the number and relative area (porosity) of intermediate or elongated pores (according to the values of elongation index) increased. As stated by Beaudet-Vidal et al. (1998) for a silt loamy and a loamy soil with ca. 10–40% of coarse material, rounded pores (with elongation

index LI = $per^2/[4\pi \cdot area]$ below 5) prevailed among small pores, and with the increase of a pore cross-sectional area the relative area of cracks (5 < LI < 10) and packing pores (LI > 10) increased. Droogers et al. (1998) estimated the averaged parameters to describe the entire pattern of the macroporosity including shape and convex shape with resolution of 330 or 440 μm per pixel. In their study of a loamy soil, pore systems with larger average pore sizes were characterized with larger values of shape index, which indicated the larger irregularity of pores (i.e. lower roundness).

It could be stated that small pore or solid phase element cross-sections revealed usually larger compactness index values. This phenomenon was closely related to the ability to distinguish the small differences in shape while evaluating objects in a photographs of soil structure in the computer program for image analysis. The shape indices do not depend, theoretically, on the cross-section's size, but the rule is only valid in the continuous Euclidean space. Due to a finite resolution of soil structure images composed of square pixels it is not possible to resolve correctly the shape of small objects. Wojnar et al. (2002) assessed via the Aphelion programme that for a circles of a diameter below 25 pixels their perimeters were underestimated and the relative error of the perimeter measurement was larger than 10% and increased with the decrease of the circle size. The relative error of the area measurement was, on the other hand, below 1%. Consequently, the authors recommend to avoid the measurement of a perimeter or length of curvilinear objects of a complicated shape. In fact, the analysis of a shape of objects below 10 pixels of equivalent diameter should not be done at all. It is therefore justified and even recommended to analyse the shape of objects larger than a specific limit value, e.g. 100 pix^2. To increase the number of pixels per object it is necessary to increase the resolution of the image. An interesting method of solving this problem by way of merging (reconstructed) multiscale images was reported by Gerke et al. (2015).

It is then an inherent feature of computer systems that small pores are mostly classified

as rounded or compact due to the finite resolution of analysed images. On the other hand, large cross-sections would be more often classified as irregular or spread or elongated, especially if the intricate cross-sections were not separated into simpler and discrete objects prior to analysis. The rules apply to any soil structure image, or, in fact, to any image on which shape analysis is based. Soil structure could be however differentiated by the distributions of pore or solid phase element cross-sections among shape index classes. Moreover, the analysis of shape of pore or solid phase element cross-sections should be accomplished for the objects of a wide range of sizes in relation to the image resolution, because in each size class there exist different distribution of shapes. Consequently, a selected and narrow size range could not reflect in a representative way the total distribution of shapes in the whole range of sizes.

Soil structure influences other soil physical attributes. In consequence some relationships should exist between geometrical characteristics of soil structure and soil air and water properties. It is well known that the soil hydraulic conductivity depend on the orientation of soil pores, their spatial arrangement and continuity (Bryk and Kołodziej, 2014; Skvortsova and Utkaeva, 2008). The geometry of soil pores is more sensitive to changes due to external conditions than some direct physical parameters, e.g. bulk density (Nimmo and Akstin, 1988; Skvortsova and Utkaeva, 2008). The shape of pores and solid phase elements could also affect the hydraulic properties but not always in a simply discernible way (Holden, 1995).

In the current paper, the interactions of area and number of objects in the compactness index classes and selected soil chemical and physical properties were studied. In Tables 6 and 7 only the strongest linear regressions ($R^2 > 0.7$) were shown for clarity. First, the influence of soil material features expressed via texture, particle density, and *TOC* on shape was estimated. The measured morphometric parameters were also related to bulk density which described the

overall compactness (in terms of the arrangement of soil groundmass) of the soil sample.

The increase of the average areas of the compact and very compact pore and solid phase element cross-sections (AN_{P3}–AN_{P6}, AN_{S3}–AN_{S6}) with the increase of clay and silt content and the decrease of sand content was noted. In fine-grained soils developed from loess even the larger objects had smoother walls than in coarser-grained sandy soils (Bryk, 2012). Their outlines were therefore less convoluted which resulted in lower perimeter values and ultimately – larger *CMP* values.

The total relative number (N_{AP}) and the relative number of pore cross-sections in the *CMP* classes (N_{AP2}–N_{AP7}) was related to the texture or particle density. The average areas in these shape classes were up to 1–2 orders of magnitude smaller than the average area of the most spread pores (A_{NP1}). It could be observed in the photographs of soil structure (Fig. 1) that the small pores in the studied soils, especially the sandy ones, resulted mainly from the arrangement of the primary mineral particles and thus were mostly governed by the texture. Some of the very compact pores ($CMP \geq 1$) increased in area and number with the increase of clay content. The larger fraction of small and round pores (so called *Nadelstichporen*) was indeed detected in the silt loamy soils developed from loess and richer in clay than sandy soils.

On the other hand, the analogous parameters measured for solid phase elements (N_{AS}, N_{AS2}–N_{AS7}) and the average area (AN_{S1}) of the most spread solid phase element cross-sections depended on *TOC* and bulk density, both values being strongly negatively correlated (R^2 = 0.721). These results confirmed that the organic matter was a strong aggregate-forming factor. The number of discrete solid phase elements including aggregates, irrespective of their shape, increased with increasing *TOC* and decreased upon consolidation revealed by the bulk density increase. The average area of the most spread (and the largest) solid phase elements decreased with the decreasing bulk density and increasing *TOC* confirming the loosening of soil and the

gradual growth of the number of discrete aggregates, which was visible in the consecutive structure photographs of A horizons: CM-eu – CH-ha – AR-br.dy – PZ-ab, and C or Ck horizons: CM-eu – CH-ha – PZ-ab – AR-br.dy (Fig. 1). At the same time, with the formation of discrete aggregates, there occurred the continuous void space visible as the spread pore cross-sections (A_{AP}, A_{AP1}, A_{AP2}, N_{AP1}).

It was studied furthermore whether the morphometric parameters in the selected compactness classes showed any relation to air and water soil properties (Tab. 7). Field water capacity (*FWC*) and available water capacity (*AWC*) increased with the decrease of the relative number of mainly compact and very compact pore cross-sections (N_{AP2}–N_{AP4}) by the decrease of the average area of the most spread solid phase element cross-sections (AN_{S1}). These results seemed quite justified, since the compact and very compact pores were mostly small and isolated from each other and as such they could reduce the space available for water or air and the decrease of AN_{S1} indicated soil loosening. On the other hand, from the physical point of view, the relation with relative area rather than the relative number of pores was expected, because the area of pores derived from soil structure images represented directly the volume of the pores. Both water capacities increased with the increasing average areas of any pore cross-sections except the most spread ones (AN_{P2}–AN_{P7}) and the average areas of the compact and very compact solid phase element cross-sections (AN_{S3}–AN_{S6}). Moreover, field air capacity, *FAC*, increased with the increase of the total relative number (NA_P) and the relative number of the compact and very compact pore cross-sections (NA_{P3}–NA_{P6}). These morphometric parameters were related to soil texture (Tab. 6), in consequence the observed relations showed indirectly the dependence of soil water and air properties (*AWC*, *FWC*, and *FAC*) on soil texture, rather than connection with the shape of pores and solid phase elements.

Field air permeability (lg*FAP*) and hydraulic conductivity (lgK_S) depended on the relative area of the majority of pore classes (A_{AP2}–A_{AP5}). The value of lgK_S increased also with

the increase of the relative number of the compact and very compact pore cross-sections (N_{AP3}–N_{AP5}). Contrary to expectation, these relations became stronger, especially for lg*FAP*, with the increasing *CMP* of pore cross-sections, i.e. when the pores became smaller and more compact and presumably more isolated from each other. The value of lg*FAP* increased with the increase of the average areas of the compact and very compact pore cross-sections (AN_{P3}–AN_{P7}). Field air permeability (lg*FAP*) depended moreover on the average area of the most spread pore cross-sections (AN_{P1}) in connection with the relative number of the majority of pore cross-section classes (N_{AP2}–N_{AP5}) or the average area of the most spread solid phase element cross-sections (AN_{S1}). Taking into account the properties of the pore cross-sections in the succeeding *CMP* classes, a straightforward relation of the air permeability with the relative area of the most spread pore cross-sections was expected. These pores tend to be the largest and the most branched, allowing for the longest path for air (or water) movement in soil. In fact, lg*FAP* depended strongly on the relative area of the most spread pore cross-sections (A_{AP1}) but this relation was also influenced by the average area of the most spread solid phase element cross-sections (AN_{S1}).

5. Conclusions

The properties of one of the most widely used shape indices were examined. The area and number of objects in the selected compactness index classes showed numerous relations to the soil physical and chemical parameters for the studied soil textures (sand, silt loam) and horizons (A, C, Ck). The relations differed for pore and solid phase element cross-sections and depended also on the object shape (spread, compact or very compact). The number distributions of structural objects among compactness index classes proved to be a useful tool for the diagnosis of soil structure status and change. The study showed moreover that the

compactness index increased with the decreasing size of the objects when measured via computer-aided image analysis. Small cross-sections revealed usually larger compactness index values, and large cross-sections were more often classified as irregular or spread. Therefore the analysis of shape of soil structural elements should encompass a wide range of element sizes in relation to the image resolution to obtain the unbiased shape distributions.

Acknowledgements

The research was financed from the budget for science in Poland in 2010–2013, grant no. N N310 447938.

References

ADCIS SA, AAI Inc., 2010. Aphelion Imaging Software Suite, version 4.0.8.

Aguilar, J., Dorronsoro-Fdez, C., Fernández, J., Dorronsoro Diaz, C., Martin, F., Dorronsoro, B., 2017. Soil Microscopy. Soil Micromorphography. Interactive Multimedia Programme for Self-studying Soil Thin Section Description. http://edafologia.ugr.es/micgraf/indexw.htm (accessed 04.07.2017).

Beaudet-Vidal, L., Fradin, V., Rossignol, J.-P., 1998. Study of the macroporosity of reconstituted anthropic soils by image analysis. Soil Till. Res. 47, 173–179. http://dx.doi.org/10.1016/S0167-1987(98)00090-7

Beckmann, W., 1962. On the micromorphometric investigation of cavities and aggregates in soils. Z. Pflanz. Düngung Bodenkunde 99, 129–139.

Bouma, J., Jongerius, A., Boersma, O., Jager, A., Schoonder-beek, D., 1977. The function of different types of macropores during saturated flow through four swelling soil horizons. Soil Sci. Soc. Am. J. 41, 945–950. http://dx.doi.org/10.2136/sssaj1977.03615995004100050028x

Bryk, M., 2008. Morphometric evaluation of transformation of soil structure from coherent into aggregate one. Acta Agrophys. 12(3), 595–606. (in Polish)

Bryk, M., 2012. Evaluation of soil aggregate surface roughness by image analysis. Soil Sci. Annu. 63(2), 9–13. http://dx.doi.org/10.2478/v10239-012-0016-1 (in Polish)

Bryk, M., Kołodziej, B., 2014. Assessment of water and air permeability of chernozem supported by image analysis. Soil Till. Res. 138, 73–84. http://dx.doi.org/10.1016/j.still.2013.12.008

Canarache, A., Vintila, I.I., Munteanu, I., 2006. Elsevier's Dictionary of Soil Science. Definitions in English with French, German, and Spanish word translations, first ed. Elsevier, Amsterdam, Boston, Heidelberg, London, New York, Oxford, Paris, San Diego, San Francisco, Singapore, Sydney, Tokyo.

Chun, H.-C., Giménez, D., Yoon, S.-W., 2008. Morphology, lacunarity and entropy of intra-aggregate pores: Aggregate size and soil management effects. Geoderma 146, 83–93. http://dx.doi.org/10.1016/j.geoderma.2008.05.018

Cnudde, V., Boone, M.N., 2013. High-resolution X-ray computed tomography in geosciences: A review of the current technology and applications. Earth-Sci. Rev. 123, 1–17. http://dx.doi.org/10.1016/j.earscirev.2013.04.003

Czachor, H., Lipiec, J., 2004. Quantification of soil macroporosity with image analysis. Int. Agrophys. 18(3), 217–223.

Droogers, P., Stein, A., Bouma, J., de Boer, G., 1998. Parameters for describing soil macroporosity derived from staining patterns. Geoderma 83, 293–308. http://dx.doi.org/10.1016/S0016-7061(98)00005-6

Garbout, A., Munkholm, L.J., Hansen, S.B., 2013. Temporal dynamics for soil aggregates determined using X-ray CT scanning. Geoderma 204–205, 15–22. http://dx.doi.org/10.1016/j.geoderma.2013.04.004

Gerke, K.M., Karsanina, M.V., Mallants, D., 2015. Universal stochastic multiscale image fusion: An example application for shale rock. Sci. Rep. 5, 15880. http://dx.doi.org/10.1038/srep15880 (2015).

Gerke, K.M., Skvortsova, E.B., Korost, D.V., 2012. Tomographic method of studying soil pore space: current perspectives and results for some Russian soils. Eurasian Soil Sci. 45, 700–709. http://dx.doi.org/10.1134/S1064229312070034

Grevers, M.C.J., de Jong, E., 1992. Soil structure changes in subsoiled Solonetzic and Chernozemic soil measured by image analysis. Geoderma 53, 289–307. http://dx.doi.org/10.1016/0016-7061(92)90060-K

Hallaire, V., Curmi, P., Duboisset, A., Lavelle, P., Pashanasi, B., 2000. Soil structure changes induced by the tropical earthworm *Pontoscolex corethrurus* and organic inputs in a Peruvian ultisol. Eur. J. Soil Biol. 36, 35–44. http://dx.doi.org/10.1016/S1164-5563(00)01048-7

Helland, J.O., Ryazanov, A.V., van Dijke, M.I.J., 2008. Characterization of pore shapes for pore network models, in: Proceedings of the 11th European Conference on the Mathematics of Oil Recovery (ECMOR XI), Bergen, Norway, 8–11 September 2008. http://dx.doi.org/10.3997/2214-4609.20146420

Holden, N.M., 1993. A two-dimensional quantification of soil ped shape. J. Soil Sci. 44, 209–219. http://dx.doi.org/10.1111/j.1365-2389.1993.tb00446.x

Holden, N.M., 1995. Temporal variation in ped shape in an old pasture soil. Catena 24, 1–11. http://dx.doi.org/10.1016/0341-8162(94)00034-C.

IUSS Working Group WRB, 2015. World Reference Base for Soil Resources 2014, update 2015. International soil classification system for naming soils and creating legends for soil maps. World Soil Resources Reports No. 106. FAO, Rome.

Kim, J.-W., Kim, D., Lindquist, W.B. 2013. A re-examination of throats. Water Resour. Res.

49, 7615–7626. http://dx.doi.org/10.1002/2013WR014254.

Lindquist, W.B., 2006. The geometry of primary drainage. J. Colloid Interf. Sci. 296, 655–668. http://dx.doi.org/10.1016/j.jcis.2005.09.041

Mason, G., Morrow, N.R., 1991. Capillary behavior of a perfectly wetting liquid in irregular triangular tubes. J. Colloid Interf. Sci. 141, 262–274. http://dx.doi.org/ 10.1016/0021-9797(91)90321-X

Miao, X., Gerke, K.M., Sizonenko, T.O., 2017. A new way to parameterize hydraulic conductances of pore elements: A step towards creating pore-networks without pore shape simplifications. Adv. Water Resour. 105, 162–172. http://dx.doi.org/10.1016/j.advwatres.2017.04.021

Nimmo, J.R., Akstin, K.C., 1988. Hydraulic conductivity of a sandy soil at low water content after compaction by various methods. Soil Sci. Soc. Am. J. 52, 303–310. http://dx.doi.org/10.2136/sssaj1988.03615995005200020001x

Øren, P.E., Bakke, S., Arntzen, O.J., 1998. Extending predictive capabilities to network models. SPE J. 3, 324–336. http://dx.doi.org/10.2118/52052-PA

Pagliai, M., Vignozzi, N., Pellegrini, S., 2004. Soil structure and the effect of management practices. Soil Till. Res. 79, 131–143. http://dx.doi.org/10.1016/j.still.2004.07.002

Panini, T., Torri, D., Pellegrini, S., Pagliai, M., Salvador Sanchis, M.P., 1997. A theoretical approach to soil porosity and sealing development using simulated rainstorms. Catena 31, 199–218. http://dx.doi.org/10.1016/S0341-8162(97)00039-8

Pardini, G., Vigna Guidi, G., Pini, R., Regüés, D., Gallart, F., 1996. Structure and porosity of smectitic mudrocks as affected by experimental wetting-drying cycles and freezing-thawing cycles. Catena 27, 149–165. http://dx.doi.org/10.1016/0341-8162(96)00024-0

Patzek, T.W., Silin, D.B., 2001. Shape factor and hydraulic conductance in noncircular capillaries I. One-phase creeping flow. J. Colloid Interf. Sci. 236, 295–304.

http://dx.doi.org/10.1006/jcis.2000.7413

Pérès, G., Cluzeau, D., Curmi, P., Hallaire, V., 1998. Earthworm activity and soil structure changes due to organic enrichments in vineyard systems. Biol. Fert. Soils 27, 417–424. http://dx.doi.org/10.1007/s003740050452

Peth, S., Horn, R., Beckmann, F., Donath, T., Fischer, J., Smucker, A.J.M. 2008. Three-dimensional quantification of intra-aggregate pore-space features using synchrotron-radiation-based microtomography. Soil Sci. Soc. Am. J. 72, 897–907. http://dx.doi.org/10.2136/sssaj2007.0130

PN-ISO 10693, 2002. Soil Quality – Determination of Carbonate Content – Volumetric Method. Polish Committee for Standardization, Warsaw.

PN-ISO 11508, 2001. Soil Quality – Determination of Particle Density. Polish Committee for Standardization, Warsaw.

PN-ISO 14235, 2003. Soil Quality – Determination of Organic Carbon by Wet Oxidation with Dichromate(VI) in Sulphuric(VI) Acid. Polish Committee for Standardization, Warsaw.

Polish Society of Soil Science, 2009. Particle size distribution and textural classes of soils and mineral materials – classification of Polish Society of Soil Science 2008. Soil Sci. Annu. 60(2), 5–16.

Puentes, R., Wilding, L.P., Drees, L.R., 1992. Microspatial variability and sampling concepts in soil porosity studies of Vertisols. Geoderma 53, 373–385. http://dx.doi.org/10.1016/0016-7061(92)90065-F

Ringrose-Voase, A.J., 1996. Measurement of soil macropore geometry by image analysis of sections through impregnated soils. Plant Soil 183, 27–47. http://dx.doi.org/10.1007/BF02185563

Sakai, N., Yonekawa, S., Matsuzaki, A., Morishima, H., 1996. Two-dimensional image

analysis of the shape of rice and its application to separating varieties. J. Food Eng. 27, 397–407. http://dx.doi.org/10.1016/0260-8774(95)00022-4

Sholokhova, Y., Kim, D., Lindquist, W.B., 2009. Network flow modeling via lattice-Boltzmann based channel conductance. Adv. Water Resour. 32, 205–212. http://dx.doi.org/10.1016/j.advwatres.2008.10.016

Skvortsova, E.B., 2009. Changes in the geometric structure of pores and aggregates as indicators of the structural degradation of cultivated soils. Eurasian Soil Sci. 42, 1254–1262. http://dx.doi.org/10.1134/S1064229309110088

Skvortsova, E.B., Morozov, D.R., 1993. Micromorphometric classification and diagnostics of the soil porous space structure. Pochvovedenie 6, 49–56.

Skvortsova, E.B., Rozhkov, V.A., Abrosimov, K.N., Romanenko, K.A., Khokhlov, S.F., Khaidapova, D.D., Klyueva, V.V., Yudina, A.V. 2016. Microtomographic analysis of pore space in a virgin soddy-podzolic soil. Eurasian Soil Sci. 49, 1250–1258. http://dx.doi.org/10.1134/S106422931611009

Skvortsova, E.B., Sanzharova, S.I., 2007. Micromorphometric features of pore space in the plow horizons of loamy soils. Eurasian Soil Sci. 40, 445–455. http://dx.doi.org/10.1134/S1064229307040114

Skvortsova, E.B., Utkaeva, V.F., 2008. Soil pore space arrangement as a geometric indicator of soil structure. Eurasian Soil Sci. 41, 1198–1204. http://dx.doi.org/10.1134/S1064229308110082

Słowińska-Jurkiewicz, A., Bryk, M., Kołodziej, B., Jaroszuk-Sierocińska, M., 2012. Macrostructure of Soils in Poland. AWR Magic, Lublin.

Vogel, H.J., Weller, U., Babel, U., 1993. Estimating orientation and width of channels and cracks at soil polished blocks – a stereological approach. Geoderma, 56, 301–316. http://dx.doi.org/10.1016/0016-7061(93)90119-6

Wojnar, L., Kurzydłowski, K.J., Szala, J., 2002. Image analysis practice, first ed. Polish Society of Stereology, Cracow. (in Polish) http://suw.biblos.pk.edu.pl/resourceDetails&rId=3964 (accessed 04.07.2017).

Zhou, H., Peng, X., Peth, S., Xiao, T.Q., 2012. Effects of vegetation restoration on soil aggregate microstructure quantified with synchrotron-based micro-computed tomography. Soil & Tillage Research 124, 17–23. http://dx.doi.org/10.1016/j.still.2012.04.006

Figure captions

Fig. 1. Soil structure of A, C and Ck horizons. Photographs of the representative soil blocks; pores are black. PZ-ab – Albic Podzol, AR-br.dy – Dystric Brunic Arenosol, CH-ha – Haplic Chernozem, CM-eu – Eutric Cambisol. Main features: a, f – roots; b, c, i – biogenic channels; d – structure with single grains and compact grains; e – sub-angular blocks; g – structure with simple packing voids and vughs; h, n – crumbs; k – planes; l, s – bioturbations; m, p, r – vughs; o – sub-angular blocks separated by planes. Further details are given in the Section 3.2. Soil structure.

Fig. 2. Pore cross-sections > 100 pix^2 extracted from a structure image of a silt loamy soil and the corresponding values of compactness index CMP_P. The proportions of cross-section sizes are maintained.

Fig. 3. Distributions of (a, c) pore or (b, d) solid phase element cross-sections among *CMP* classes according to number (N_{APk}/N_{AP} or N_{ASk}/N_{AS}, %) or area (A_{APk}/A_{AP} or A_{ASk}/A_{AS}, %).

Fig. 4. Relation between relative number and relative area, lgN_{Ak} vs. lgA_{Ak} (solid black line with a 95% confidence interval marked with grey), and average area of a cross-section, AN_k in mm^2 (circles) for (a) pore and (b) solid phase element cross-sections > 100 pix^2 in *CMP* classes *k*. The numbers above small and large circles represent the lower and the upper limits, respectively, of the average area of a cross-section.

Fig. 5. Compactness index, lgCMP_{Pi}, as a function of area, lgA_{Pi}, of a pore cross-section > 100 pix^2. PZ – Albic Podzol, AR – Dystric Brunic Arenosol, CH – Haplic Chernozem, CM – Eutric Cambisol.

Fig. 6. Compactness index, lgCMP_{Si}, as a function of area, lgA_{Si}, of a solid phase element cross-section > 100 pix^2. PZ – Albic Podzol, AR – Dystric Brunic Arenosol, CH – Haplic Chernozem, CM – Eutric Cambisol.

VoR: https://doi.org/10.1016/j.geoderma.2017.12.030

Table 1. Characteristics of sampling sites

Soil	Albic Podzol (PZ-ab)		Dystric Brunic Arenosol (AR-br.dy)		Haplic Chernozem (CH-ha)		Eutric Cambisol (CM-eu)	
Coordinates	50°25’26” N, 22°12’30” E		50°32’16” N, 22°56’43” E		50°30’39” N, 23°56’05” E		50°29’43” N, 23°37’03” E	
Locality	Doliny near San River		Tereszpol-Kukiełki		Marysin Kolonia		Wola Gródecka	
Physiographic region	512.45 The Tarnobrzeska Plain		512.47 The Biłgorajska Plain		851.13 The Sokalska Hills			
Parent material	Eolian sand		Glacio-fluvial sand		Loess		Loess	
Vegetation / Plant community	Mixed forest of Scots pine *Pinus sylvestris* and pedunculate oak *Quercus robur* / *Querco roboris-Pinetum* (W.Mat. 1981) J.Mat. 1988		Nemoral Scots pine (*Pinus sylvestris*) forest / *Leucobryo-Pinetum* W.Mat. (1962)1973		Mesophytic deciduous forest of oak *Quercus robur* and *Quercus petraea*, hornbeam *Carpinus betulus*, and lime *Tilia cordata* / *Tilio cordatae-Carpinetum betuli* Tracz. 1962			
Horizon depths (cm)	O	0–6/11	O	0–5	O	0–2	O	0–5
	A	6/11–27/30	A	5–12/15	A	2–50/75	A	5–10/15
	Es	27/30–34/42	A/B	12/15–23	AC	50/75–85/135	AB	10/15–30/45
	Bhs	34/42–65/75	Bwo	23–53/73	Ck	> 85/135	Bw	30/45–67
	BC	65/75–90	C	> 53/73			BC	67–85
	C	> 90					C	85–120/135
							Ck	> 120/135

VoR: https://doi.org/10.1016/j.geoderma.2017.12.030

Table 2. Selected physical and chemical properties of the studied soils. PZ-ab – Albic Podzol, AR-br.dy – Dystric Brunic Arenosol, CH-ha – Haplic Chernozem, CM-eu – Eutric Cambisol

Sample	PZ-ab2	AR-br.dy2	CH-ha1	CM-eu2	PZ-ab7	AR-br.dy5	CH-ha5	CM-eu7
Horizon	A	A	A	A	C	C	Ck	Ck
Horizon depth (cm)	6/11–27/30	5–12/15	2–50/75	5–10/15	> 90	> 53/73	> 85/135	> 120/135
Sampling layer (cm)	16–24	5–13	2–10	6–14	106–114	80–88	120–128	138–146
Sand, c_s (g g^{-1})	0.905	0.950	0.140	0.210	0.990	0.995	0.120	0.130
Silt, c_{si} (g g^{-1})	0.090	0.050	0.710	0.720	0.000	0.050	0.740	0.750
Clay, c_c (g g^{-1})	0.005	0.000	0.150	0.070	0.010	0.000	0.140	0.120
TOC (mg g^{-1})	22.8±0.6[a]	14.9±0.5	15.9±0.2	26.3±0.1	4.2±0.3	1.6±0.0	2.3±0.4	3.5±0.7
$CaCO_3$ (mg g^{-1})	0	0	0	0	0	0	104±1	110±9
Bulk density, ρ_d (g cm^{-3})	1.16±0.09[a]	1.29±0.09	0.88±0.12	0.88±0.13	1.75±0.07	1.63±0.05	1.46±0.11	1.45±0.05
Particle density, ρ_s (g cm^{-3})	2.46±0.02[a]	2.56±0.01	2.62±0.01	2.55±0.01	2.65±0.00	2.66±0.00	2.73±0.01	2.65±0.01

[a] ± standard deviation

VoR: https://doi.org/10.1016/j.geoderma.2017.12.030

Table 3. Results of 2-way ANOVA (horizon×texture) for selected physical and chemical properties of the studied soils: c_s, c_{si}, c_c – sand, silt, and clay content; ρ_s, ρ_d – particle and bulk density; P_O – total porosity; *MWC* – maximum water capacity; *FWC* – field water capacity; *PWP* – permanent wilting point; *AWC* – available water capacity; *FAC* – field air capacity; *TOC* – total organic carbon; *FAP* – field air permeability; K_S – saturated hydraulic conductivity. X_H, X_T, underlined value – horizon, texture and overall mean, respectively. Different letters for each parameter denote statistically different values at $P < 0.05$ for horizon×texture (a–d), textures (A, B), and horizons (C, D) according to the Tukey's honestly significant difference test.

c_s (g g^{-1})

	sand	silt loam	X_H
A	0.927 a	0.175 a	0.551 C
C, Ck	0.992 a	0.125 a	0.559 C
X_T	0.960 B	0.150 A	0.555

c_{si} (g g^{-1})

	sand	silt loam	X_H
A	0.070 a	0.715 a	0.392 C
C, Ck	0.025 a	0.745 a	0.385 C
X_T	0.047 A	0.730 B	0.389

c_c (g g^{-1})

	sand	silt loam	X_H
A	0.002 a	0.110 a	0.056 C
C, Ck	0.005 a	0.130 a	0.067 C
X_T	0.004 A	0.120 B	0.062

ρ_s (g cm^{-3})

	sand	silt loam	X_H
A	2.51 a	2.58 a	2.55 C
C, Ck	2.65 a	2.69 a	2.67 D
X_T	2.58 A	2.64 B	2.61

ρ_d (g cm^{-3})

	sand	silt loam	X_H
A	1.23 a	0.88 a	1.05 C
C, Ck	1.69 a	1.46 a	1.57 D
X_T	1.46 B	1.17 A	1.31

P_O (cm^3 cm^{-3})

	sand	silt loam	X_H
A	0.512 a	0.660 a	0.586 D
C, Ck	0.363 a	0.459 a	0.411 C
X_T	0.438 A	0.559 B	0.498

MWC (cm^3 cm^{-3})

	sand	silt loam	X_H
A	0.435 a	0.615 a	0.525 D
C, Ck	0.379 a	0.529 a	0.454 C
X_T	0.407 A	0.572 B	0.490

FWC (cm^3 cm^{-3})

	sand	silt loam	X_H
A	0.244 b	0.366 c	0.305
C, Ck	0.084 a	0.397 d	0.240
X_T	0.164	0.381	0.273

PWP (cm^3 cm^{-3})

	sand	silt loam	X_H
A	0.065 b	0.072 b	0.069
C, Ck	0.009 a	0.080 b	0.044
X_T	0.037	0.076	0.056

AWC (cm^3 cm^{-3})

	sand	silt loam	X_H
A	0.179 a	0.294 a	0.236 C
C, Ck	0.075 a	0.317 a	0.196 C
X_T	0.127 A	0.305 B	0.216

FAC (cm^3 cm^{-3})

	sand	silt loam	X_H
A	0.191 ab	0.249 bc	0.220
C, Ck	0.296 c	0.132 a	0.214
X_T	0.243	0.191	0.217

TOC (mg g^{-1})

	sand	silt loam	X_H
A	18.8 a	21.1 a	19.9 D
C, Ck	2.9 a	2.9 a	2.9 C
X_T	10.9 A	12.0 A	11.4

FAP (10^{-8} × m^2 Pa^{-1} s^{-1})

	sand	silt loam	X_H
A	24.1 b	225.3 c	73.7
C, Ck	87.8 bc	2.7 a	15.4
X_T	46	24.6	33.7

K_S (cm h^{-1})

	sand	silt loam	X_H
A	23.6 b	29.5 b	26.4
C, Ck	38.1 b	0.3 a	3.2
X_T	30	2.8	9.2

VoR: https://doi.org/10.1016/j.geoderma.2017.12.030

Table 4. Results of 2-way ANOVA (horizon×texture) for morphometric parameters of pore cross-sections > 100 pix^2: N_{AP1}–N_{AP7} – relative number in *CMP* classes; N_{AP} – total relative number; A_{AP1}–A_{AP7} – relative area in *CMP* classes; A_{AP} – total relative area; AN_{P1}–AN_{P7} – average area in *CMP* classes. X_H, X_T, underlined value – horizon, texture and overall mean, respectively. Different letters for each parameter denote statistically different values at $P < 0.05$ for horizon×texture (a–c), textures (A, B), and horizons (C, D) according to the Tukey's honestly significant difference test.

N_{AP1} (dm^{-2})	sand	silt loam	X_H
A	393.9 c	204.7 b	299.3
C, Ck	125.7 ab	83.6 a	104.7
X_T	259.8	144.2	202.0

A_{AP1} (cm^2 dm^{-2})	sand	silt loam	X_H
A	5.91 b	24.15 c	15.03
C, Ck	0.68 a	2.32 ab	1.50
X_T	3.29	13.24	8.26

AN_{P1} (mm^2)	sand	silt loam	X_H
A	1.528 a	14.361 b	7.944
C, Ck	0.528 a	2.758 a	1.643
X_T	1.028	8.559	4.794

N_{AP2} (dm^{-2})	sand	silt loam	X_H
A	1107.3 a	565.1 a	836.2 D
C, Ck	759.1 a	214.3 a	486.7 C
X_T	933.2 B	389.7 A	661.5

A_{AP2} (cm^2 dm^{-2})	sand	silt loam	X_H
A	1.59 a	1.18 a	1.39 D
C, Ck	0.88 a	0.43 a	0.66 C
X_T	1.24 B	0.81 A	1.02

AN_{P2} (mm^2)	sand	silt loam	X_H
A	0.159 a	0.235 a	0.197 C
C, Ck	0.126 a	0.219 a	0.173 C
X_T	0.143 A	0.227 B	0.185

N_{AP3} (dm^{-2})	sand	silt loam	X_H
A	1008.2 c	574.9 b	791.6
C, Ck	905.5 c	212.5 a	559.0
X_T	956.9	393.7	675.3

A_{AP3} (cm^2 dm^{-2})	sand	silt loam	X_H
A	0.82 c	0.63 b	0.72
C, Ck	0.66 bc	0.24 a	0.45
X_T	0.74	0.43	0.59

AN_{P3} (mm^2)	sand	silt loam	X_H
A	0.090 a	0.120 a	0.105 C
C, Ck	0.080 a	0.121 a	0.101 C
X_T	0.085 A	0.121 B	0.103

N_{AP4} (dm^{-2})	sand	silt loam	X_H
A	520.6 c	344.7 b	432.7
C, Ck	509.0 c	152.7 a	330.9
X_T	514.8	248.7	381.8

A_{AP4} (cm^2 dm^{-2})	sand	silt loam	X_H
A	0.35 b	0.32 b	0.34
C, Ck	0.33 b	0.14 a	0.24
X_T	0.34	0.23	0.28

AN_{P4} (mm^2)	sand	silt loam	X_H
A	0.074 a	0.101 a	0.088 C
C, Ck	0.071 a	0.101 a	0.086 C
X_T	0.072 A	0.101 B	0.087

N_{AP5} (dm^{-2})	sand	silt loam	X_H
A	223.4 bc	195.7 b	209.6
C, Ck	256.2 c	107.2 a	181.7
X_T	239.8	151.4	195.6

A_{AP5} (cm^2 dm^{-2})	sand	silt loam	X_H
A	0.13 ab	0.16 b	0.15
C, Ck	0.15 b	0.09 a	0.12
X_T	0.14	0.13	0.14

AN_{P5} (mm^2)	sand	silt loam	X_H
A	0.066 a	0.089 a	0.078 C
C, Ck	0.067 a	0.093 a	0.080 C
X_T	0.066 A	0.091 B	0.079

N_{AP6} (dm^{-2})	sand	silt loam	X_H
A	53.1 a	85.4 a	69.3 C
C, Ck	97.7 a	100.2 a	99.0 D
X_T	75.4 A	92.8 B	84.1

A_{AP6} (cm^2 dm^{-2})	sand	silt loam	X_H
A	0.03 a	0.06 a	0.05 C
C, Ck	0.06 a	0.07 a	0.07 D
X_T	0.04 A	0.07 B	0.06

AN_{P6} (mm^2)	sand	silt loam	X_H
A	0.062 a	0.080 a	0.071 C
C, Ck	0.066 a	0.082 a	0.074 C
X_T	0.064 A	0.081 B	0.072

N_{AP7} (dm^{-2})	sand	silt loam	X_H
A	2.1 a	9.2 a	5.6
C, Ck	5.7 a	25.2 b	15.5
X_T	3.9	17.2	10.6

A_{AP7} (cm^2 dm^{-2})	sand	silt loam	X_H
A	0.00 a	0.01 ab	0.00
C, Ck	0.00 a	0.02 b	0.01
X_T	0.00	0.01	0.01

AN_{P7} (mm^2)	sand	silt loam	X_H
A	0.033 a	0.069 a	0.051 C
C, Ck	0.050 a	0.070 a	0.060 C
X_T	0.041 A	0.070 B	0.056

N_{AP} (dm^{-2})	sand	silt loam	X_H
A	3308.7 a	1979.7 a	2644.2 D
C, Ck	2659.0 a	895.7 a	1777.4 C
X_T	2983.9 B	1437.7 A	2210.8

A_{AP} (cm^2 dm^{-2})	sand	silt loam	X_H
A	8.82 b	26.51 c	17.66
C, Ck	2.78 a	3.32 a	3.05
X_T	5.80	14.91	10.35

VoR: https://doi.org/10.1016/j.geoderma.2017.12.030

Table 5. Results of 2-way ANOVA (horizon×texture) for morphometric parameters of solid phase element cross-sections > 100 pix^2: N_{AS1}–N_{AS7} – relative number in *CMP* classes; N_{AS} – total relative number; A_{AS1}–A_{AS7} – relative area in *CMP* classes; A_{AS} – total relative area; AN_{S1}–AN_{S7} – average area in *CMP* classes. X_H, X_T, underlined value – horizon, texture and overall mean, respectively. Different letters for each parameter denote statistically different values at P < 0.05 for horizon×texture (a–d), textures (A, B), and horizons (C, D) according to the Tukey's honestly significant difference test.

N_{AS1} (dm^{-2})

	sand	silt loam	X_H
A	19.7 a	144.9 b	82.3
C, Ck	1.7 a	9.6 a	5.6
X_T	10.7	77.2	44.0

A_{AS1} (cm^2 dm^{-2})

	sand	silt loam	X_H
A	86.92 b	67.48 a	77.20
C, Ck	93.76 c	95.03 c	94.39
X_T	90.34	81.25	85.80

AN_{S1} (mm^2)

	sand	silt loam	X_H
A	1399.983 b	122.123 a	761.053
C, Ck	6401.426 d	2583.777 c	4492.602
X_T	3900.705	1352.950	2626.827

N_{AS2} (dm^{-2})

	sand	silt loam	X_H
A	56.4 a	254.2 b	155.3
C, Ck	1.9 a	18.7 a	10.3
X_T	29.1	136.5	82.8

A_{AS2} (cm^2 dm^{-2})

	sand	silt loam	X_H
A	0.15 a	1.14 b	0.65
C, Ck	0.00 a	0.10 a	0.05
X_T	0.08	0.62	0.35

AN_{S2} (mm^2)

	sand	silt loam	X_H
A	0.380 a	0.677 a	0.529 D
C, Ck	0.080 a	0.400 a	0.240 C
X_T	0.230 A	0.539 B	0.384

N_{AS3} (dm^{-2})

	sand	silt loam	X_H
A	71.9 a	270.1 b	171.0
C, Ck	2.7 a	16.1 a	9.4
X_T	37.3	143.1	90.2

A_{AS3} (cm^2 dm^{-2})

	sand	silt loam	X_H
A	0.09 a	0.55 b	0.32
C, Ck	0.00 a	0.06 a	0.03
X_T	0.05	0.30	0.17

AN_{S3} (mm^2)

	sand	silt loam	X_H
A	0.167 a	0.282 a	0.224 C
C, Ck	0.056 a	0.326 a	0.191 C
X_T	0.111 A	0.304 B	0.208

N_{AS4} (dm^{-2})

	sand	silt loam	X_H
A	57.2 a	220.8 b	139.0
C, Ck	4.7 a	14.5 a	9.6
X_T	31.0	117.7	74.3

A_{AS4} (cm^2 dm^{-2})

	sand	silt loam	X_H
A	0.06 a	0.33 b	0.20
C, Ck	0.00 a	0.04 a	0.02
X_T	0.03	0.18	0.11

AN_{S4} (mm^2)

	sand	silt loam	X_H
A	0.134 a	0.202 a	0.168 C
C, Ck	0.059 a	0.200 a	0.129 C
X_T	0.097 A	0.201 B	0.149

N_{AS5} (dm^{-2})

	sand	silt loam	X_H
A	42.9 a	163.0 b	103.0
C, Ck	4.0 a	10.9 a	7.4
X_T	23.5	86.9	55.2

A_{AS5} (cm^2 dm^{-2})

	sand	silt loam	X_H
A	0.03 a	0.19 b	0.11
C, Ck	0.00 a	0.01 a	0.01
X_T	0.02	0.10	0.06

AN_{S5} (mm^2)

	sand	silt loam	X_H
A	0.086 a	0.147 a	0.117 D
C, Ck	0.052 a	0.108 a	0.080 C
X_T	0.069 A	0.128 B	0.098

N_{AS6} (dm^{-2})

	sand	silt loam	X_H
A	26.7 a	95.7 b	61.2
C, Ck	3.9 a	6.5 a	5.2
X_T	15.3	51.1	33.2

A_{AS6} (cm^2 dm^{-2})

	sand	silt loam	X_H
A	0.02 a	0.08 b	0.05
C, Ck	0.00 a	0.01 a	0.01
X_T	0.01	0.05	0.03

AN_{S6} (mm^2)

	sand	silt loam	X_H
A	0.079 a	0.102 a	0.091 C
C, Ck	0.056 a	0.165 a	0.111 C
X_T	0.068 A	0.133 A	0.101

N_{AS7} (dm^{-2})

	sand	silt loam	X_H
A	5.5 a	9.1 a	7.3 D
C, Ck	0.8 a	0.5 a	0.6 C
X_T	3.2 A	4.8 A	4.0

A_{AS7} (cm^2 dm^{-2})

	sand	silt loam	X_H
A	0.00	0.01	0.00
C, Ck	0.00	0.00	0.00
X_T	0.00	0.00	0.00

AN_{S7} (mm^2)

	sand	silt loam	X_H
A	0.078 a	0.074 a	0.076 D
C, Ck	0.021 a	0.016 a	0.018 C
X_T	0.050 A	0.045 A	0.047

N_{AS} (dm^{-2})

	sand	silt loam	X_H
A	280.5 a	1157.9 b	719.2
C, Ck	19.6 a	76.9 a	48.2
X_T	150.1	617.4	373.7

A_{AS} (cm^2 dm^{-2})

	sand	silt loam	X_H
A	87.29 b	69.78 a	78.53
C, Ck	93.76 c	95.25 c	94.51
X_T	90.53	82.51	86.52

 VoR: https://doi.org/10.1016/j.geoderma.2017.12.030

Table 6. Relations of morphometric parameters vs. selected physical and chemical properties: A_{AP1}–A_{AP7} and A_{AS1} – relative area of pore or solid phase element cross-sections in *CMP* classes; A_{AP} and A_{AS} – total relative area of pore or solid phase element cross-sections; N_{AP1}–N_{AP7} and N_{AS2}–N_{AS7} – relative number of pore or solid phase element cross-sections in *CMP* classes; N_{AP} and N_{AS} – total relative number of pore or solid phase element cross-sections; AN_{P3}–AN_{P6} and AN_{S1}–AN_{S7} – average area of pore or solid phase element cross-sections in *CMP* classes; c_s, c_{si}, c_c – sand, silt, and clay content; ρ_s, ρ_d – particle and bulk density; *TOC* – total organic carbon.

Single or multiple linear regression equations	R^2	P	Single or multiple linear regression equations	R^2	P
$A_{AP1} = 45.8^{***} - 28.6^{**} \rho_d$	0.843	0.0013	$A_{AS1} = 0.72^{*} TOC + 58.7^{***} \rho_d$	0.994	< 0.0001
$A_{AP1} = 0.74^{**} TOC$	0.757	0.0023	$A_{AS} = 8.0\times10^{-3*} TOC + 0.59^{***} \rho_d$	0.994	< 0.0001
$A_{AP2} = 0.04^{*} TOC + 0.22^{*} \rho_s$	0.913	0.0006	$N_{AS2} = 8.5^{**} TOC$	0.701	0.0049
$A_{AP6} = 0.02^{**} \rho_s + 0.23^{*} c_c$	0.956	0.0001	$N_{AS3} = 9.2^{**} TOC$	0.743	0.0028
$A_{AP7} = 0.11^{***} c_c$	0.811	0.0009	$N_{AS4} = 7.5^{**} TOC$	0.753	0.0024
$A_{AP} = 0.49^{***} - 0.30^{**} \rho_d$	0.849	0.0011	$N_{AS5} = 5.4^{**} TOC$	0.780	0.0016
$A_{AP} = 8.7\times10^{-3***} TOC$	0.818	0.0008	$N_{AS5} = 313.9^{**} - 197.1^{**} \rho_d$	0.702	0.0094
$N_{AP1} = 4271.6^{***} - 1559.2^{***} \rho_s$	0.861	0.0009	$N_{AS6} = 3.2^{***} TOC$	0.809	0.0010
$N_{AP1} = 15.0^{***} TOC$	0.834	0.0006	$N_{AS6} = 183.7^{**} - 114.7^{**} \rho_d$	0.768	0.0043
$N_{AP2} = 8148.7^{***} - 564.4^{**} c_{si} - 2785.8^{**} \rho_s$	0.953	0.0005	$N_{AS7} = 0.38^{***} TOC$	0.958	< 0.0001
$N_{AP2} = 7481.4^{**} + 482.17^{**} c_s - 2715.5^{**} \rho_s$	0.946	0.0007	$N_{AS7} = 7.4^{**} \rho_s - 11.7^{*} \rho_d$	0.824	0.0054
$N_{AP2} = - 4545.5^{*} c_c + 359.2^{***} \rho_s$	0.907	0.0008	$N_{AS7} = 18.8^{**} - 11.3^{**} \rho_d$	0.740	0.0061
$N_{AP3} = 1035.0^{***} c_s$	0.910	0.0001	$N_{AS} = 38.8^{**} TOC$	0.738	0.0030
$N_{AP3} = 984.5^{***} - 807.1^{**} c_{si}$	0.783	0.0035	$AN_{S1} = 3079.2^{***} \rho_d - 117.7^{*} TOC$	0.880	0.0017
$N_{AP3} = 949.9^{***} - 4438.4^{**} c_c$	0.755	0.0051	$AN_{S3} = 2.5^{***} c_c$	0.872	0.0002
$N_{AP4} = 562.7^{***} c_s$	0.884	0.0002	$AN_{S3} = 0.43^{***} c_{si}$	0.853	0.0004
$N_{AP5} = 268.2^{***} c_s$	0.813	0.0009	$AN_{S3} = 0.35^{***} - 0.25^{**} c_s$	0.744	0.0058
$N_{AP6} = 32.4^{***} \rho_s$	0.944	< 0.0001	$AN_{S4} = 0.28^{**} c_{si}$	0.771	0.0018
$N_{AP7} = 146.5^{***} c_c$	0.840	0.0005	$AN_{S4} = 1.6^{**} c_c$	0.760	0.0022
$N_{AP} = 1958.9^{*} c_s + 425.4^{*} \rho_s$	0.947	0.0001	$AN_{S5} = 0.18^{**} c_{si}$	0.751	0.0025
$AN_{P3} = 0.08^{***} + 0.31^{**} c_c$	0.846	0.0012	$AN_{S5} = 1.1^{**} c_c$	0.744	0.0027
$AN_{P4} = 0.07^{***} + 0.26^{***} c_c$	0.879	0.0006	$AN_{S6} = 1.1^{**} c_c$	0.783	0.0015
$AN_{P5} = 0.07^{***} + 0.21^{***} c_c$	0.893	0.0004	$AN_{S6} = 0.19^{**} c_{si}$	0.763	0.0021
$AN_{P6} = 0.06^{***} + 0.14^{**} c_c$	0.850	0.0011	$AN_{S7} = 3.6\times10^{-3***} TOC$	0.876	0.0002

*, **, *** significance levels for linear regression coefficients.

 VoR: https://doi.org/10.1016/j.geoderma.2017.12.030

Table 7. Relations of water and air properties vs. morphometric parameters: *FWC* – field water capacity; *FAC* – field air capacity; K_S – saturated hydraulic conductivity; *AWC* – available water capacity; *FAP* – field air permeability; A_{AP1}–A_{AP5} and A_{AS1} – relative area of pore or solid phase element cross-sections in *CMP* classes; A_{AS} – total relative area of solid phase element cross-sections; N_{AP2}–N_{AP6} – relative number of pore cross-sections in *CMP* classes; N_{AP} – total relative number of pore cross-sections; AN_{P1}–AN_{P7} and AN_{S1}–AN_{S6} – average area of pore or solid phase element cross-sections in *CMP* classes.

Single or multiple linear regression equations	R^2	P	Single or multiple linear regression equations	R^2	P
$FWC = 0.52^{***} - 2.3\times10^{-4***} N_{AP3} - 3.4\times10^{-5***} AN_{S1}$	0.974	0.0001	$AWC = 0.41^{***} - 1.7\times10^{-4*} N_{AP2} - 3.1\times10^{-5**} AN_{S1}$	0.889	0.0041
$FWC = 0.54^{***} - 4.8\times10^{-4***} N_{AP4} - 3.3\times10^{-5***} AN_{S1}$	0.968	0.0002	$AWC = 0.42^{***} - 2.0\times10^{-4**} N_{AP3} - 2.5\times10^{-5**} AN_{S1}$	0.937	0.0010
$FWC = 0.58^{***} - 1.2\times10^{-3**} N_{AP5} - 3.1\times10^{-5**} AN_{S1}$	0.915	0.0021	$AWC = 0.44^{***} - 4.3\times10^{-4**} N_{AP4} - 2.4\times10^{-5**} AN_{S1}$	0.952	0.0005
$FWC = 1.50^{***} AN_{P2}$	0.935	< 0.0001	$AWC = 0.49^{***} - 1.1\times10^{-3**} N_{AP5} - 2.2\times10^{-5*} AN_{S1}$	0.919	0.0018
$FWC = 2.74^{***} AN_{P3}$	0.926	< 0.0001	$AWC = 1.18^{***} AN_{P2}$	0.913	0.0001
$FWC = 3.23^{***} AN_{P4}$	0.915	0.0001	$AWC = 2.16^{***} AN_{P3}$	0.907	0.0001
$FWC = 3.57^{***} AN_{P5}$	0.910	0.0001	$AWC = 2.54^{***} AN_{P4}$	0.897	0.0001
$FWC = 3.85^{***} AN_{P6}$	0.889	0.0001	$AWC = 2.82^{***} AN_{P5}$	0.896	0.0001
$FWC = 4.88^{***} AN_{P7}$	0.894	0.0001	$AWC = 3.06^{***} AN_{P6}$	0.881	0.0002
$FWC = 1.22^{***} AN_{S3}$	0.942	< 0.0001	$AWC = 3.89^{***} AN_{P7}$	0.898	0.0001
$FWC = 1.74^{***} AN_{S4}$	0.934	< 0.0001	$AWC = 0.95^{***} AN_{S3}$	0.896	0.0001
$FWC = 2.68^{***} AN_{S5}$	0.918	< 0.0001	$AWC = 1.36^{***} AN_{S4}$	0.904	0.0001
$FWC = 2.56^{***} AN_{S6}$	0.903	0.0001	$AWC = 2.10^{***} AN_{S5}$	0.882	0.0002
$FAC = 0.34^{***} A_{AP3}$	0.861	0.0003	$AWC = 2.01^{***} AN_{S6}$	0.875	0.0002
$FAC = 0.72^{***} A_{AP4}$	0.899	0.0001	$\lg FAP = 0.10^{**} A_{AP1} + 2.7\times10^{-4**} AN_{S1}$	0.889	0.0014
$FAC = 1.55^{***} A_{AP5}$	0.926	< 0.0001	$\lg FAP = 1.38^{**} A_{AP2}$	0.797	0.0012
$FAC = 2.8\times10^{-4***} N_{AP3}$	0.828	0.0007	$\lg FAP = 2.57^{***} A_{AP3}$	0.866	0.0003
$FAC = 5.2\times10^{-4***} N_{AP4}$	0.874	0.0002	$\lg FAP = 5.52^{***} A_{AP4}$	0.911	0.0001
$FAC = 1.1\times10^{-3***} N_{AP5}$	0.941	< 0.0001	$\lg FAP = 11.80^{***} A_{AP5}$	0.935	< 0.0001
$FAC = 2.4\times10^{-3***} N_{AP6}$	0.861	0.0003	$\lg FAP = 0.16^{**} AN_{P1} + 2.7\times10^{-4*} AN_{S1}$	0.865	0.0024
$FAC = 8.7\times10^{-5***} N_{AP}$	0.820	0.0008	$\lg FAP = 0.11^{*} AN_{P1} + 1.4\times10^{-3*} N_{AP2}$	0.864	0.0025
$FAC = 2.5\times10^{-3***} A_{AS1}$	0.868	0.0003	$\lg FAP = 0.10^{*} AN_{P1} + 1.6\times10^{-3**} N_{AP3}$	0.919	0.0005
$FAC = 0.25^{***} A_{AS}$	0.871	0.0002	$\lg FAP = 0.09^{*} AN_{P1} + 3.0\times10^{-3**} N_{AP4}$	0.934	0.0003
$\lg K_S = 1.1^{**} A_{AP2}$	0.707	0.0045	$\lg FAP = 0.07^{*} AN_{P1} + 6.5\times10^{-3***} N_{AP5}$	0.952	0.0001
$\lg K_S = 1.9^{**} A_{AP3}$	0.777	0.0017	$\lg FAP = 14.3^{**} AN_{P3}$	0.745	0.0027
$\lg K_S = 3.9^{**} A_{AP4}$	0.758	0.0023	$\lg FAP = 17.0^{**} AN_{P4}$	0.758	0.0022
$\lg K_S = 8.0^{**} A_{AP5}$	0.706	0.0046	$\lg FAP = 18.7^{**} AN_{P5}$	0.745	0.0027
$\lg K_S = 1.6\times10^{-3**} N_{AP3}$	0.764	0.0021	$\lg FAP = 20.6^{**} AN_{P6}$	0.754	0.0024
$\lg K_S = 2.9\times10^{-3**} N_{AP4}$	0.763	0.0021	$\lg FAP = 25.2^{**} AN_{P7}$	0.710	0.0043
$\lg K_S = 5.7\times10^{-3**} N_{AP5}$	0.753	0.0024			

*, **, *** significance levels for linear regression coefficients.

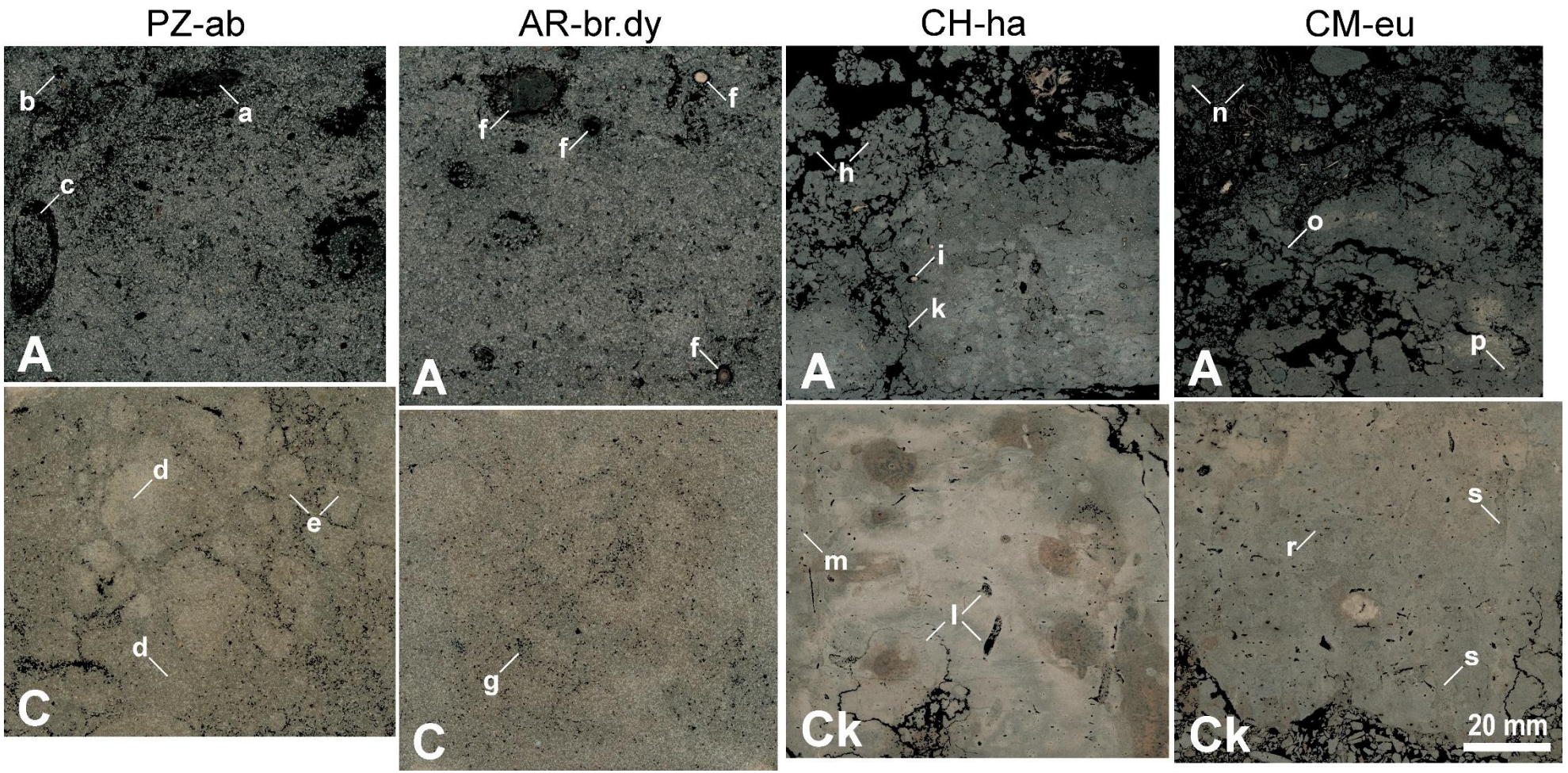
PZ-ab
AR-br.dy
CH-ha
CM-eu
b
a
c
A
f
f
f
f
A
h
i
k
A
n
o
p
A
d
e
d
C
g
C
m
l
Ck
s
r
s
Ck
20 mm

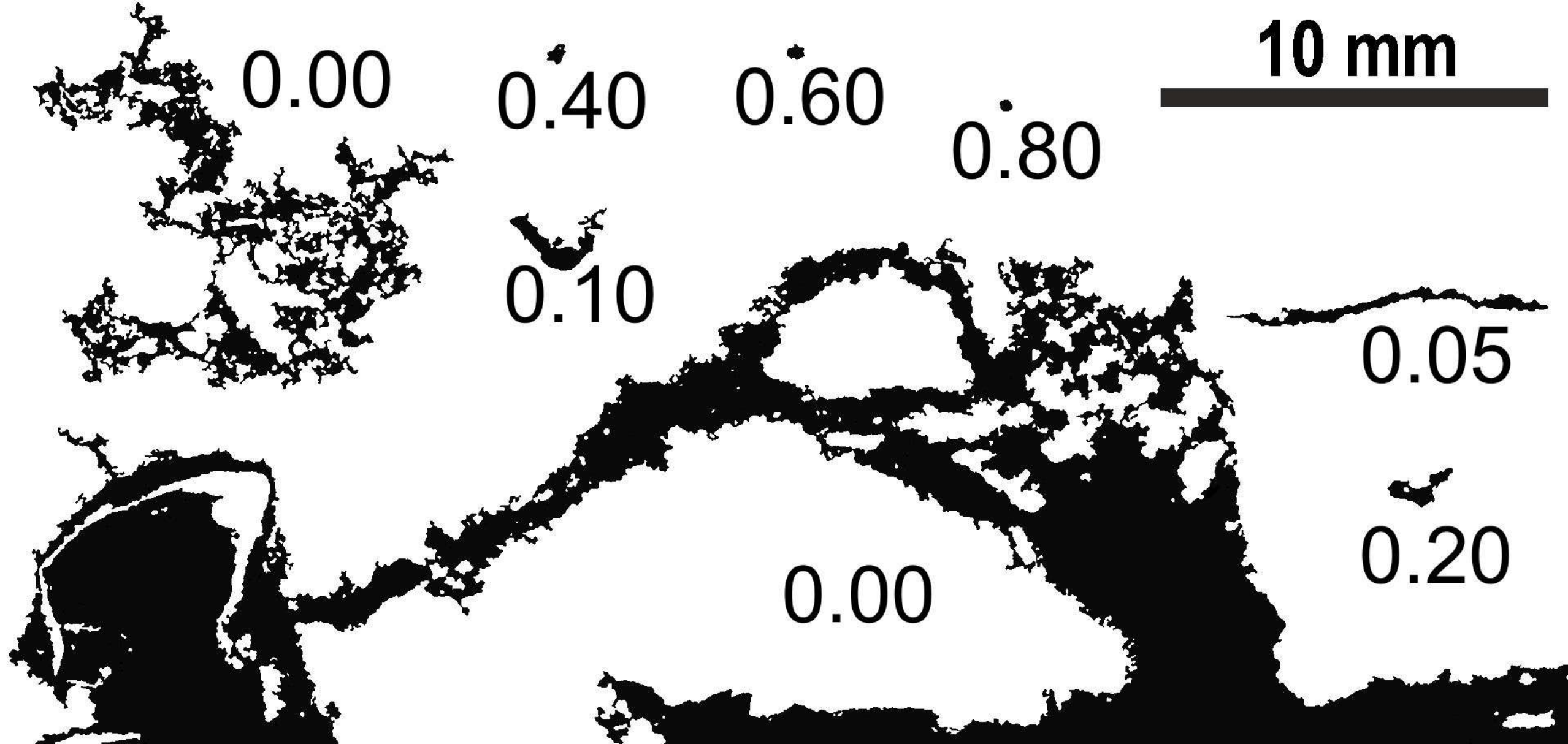
0.00
0.40
0.60
0.80
10 mm
0.10
0.05
0.20
0.00

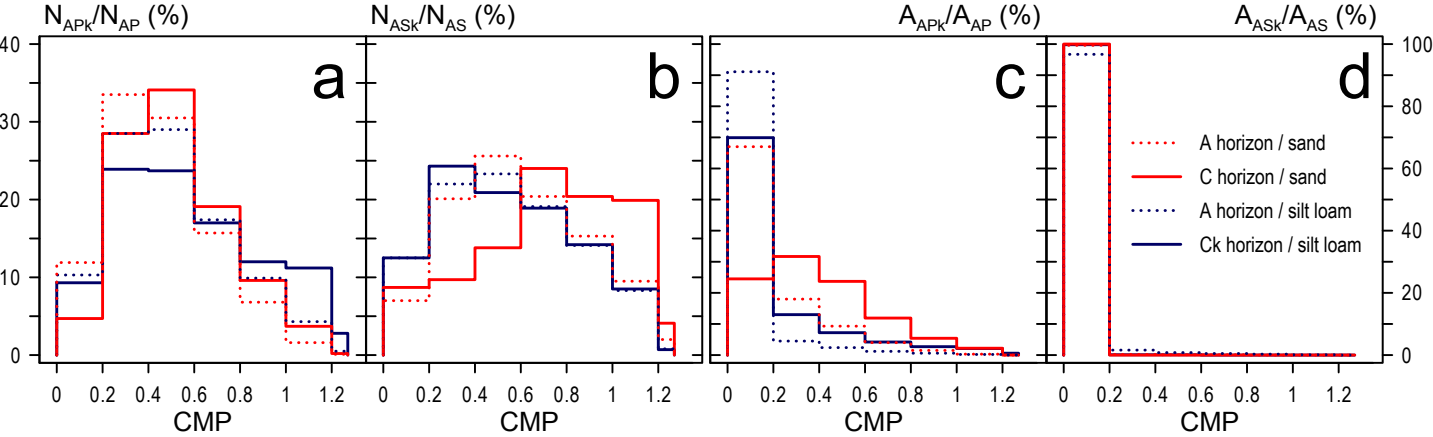
N_{APk}/N_{AP} (%)
N_{ASk}/N_{AS} (%)
A_{APk}/A_{AP} (%)
A_{ASk}/A_{AS} (%)
a
b
c
d
A horizon / sand
C horizon / sand
A horizon / silt loam
Ck horizon / silt loam
CMP
CMP
CMP
CMP

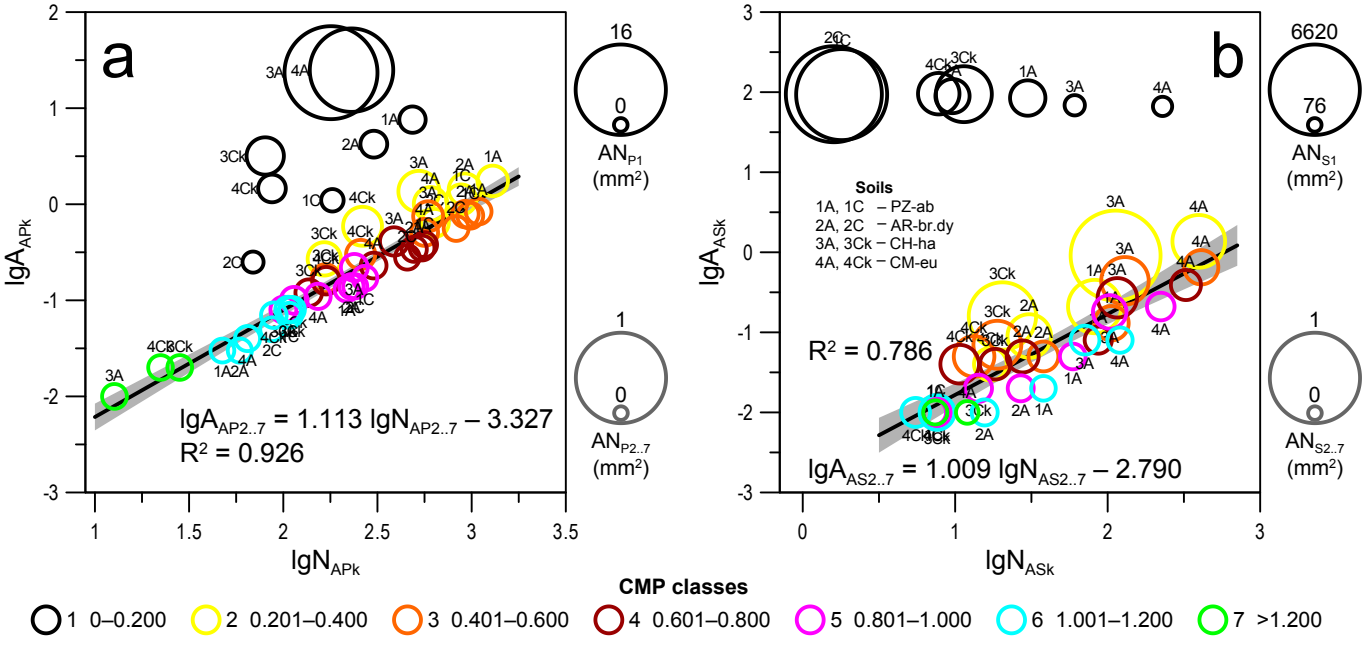
a
b
lgA_APk
lgN_APk
lgA_ASk
lgN_ASk
lgA_AP2..7 = 1.113 lgN_AP2..7 – 3.327
R² = 0.926
lgA_AS2..7 = 1.009 lgN_AS2..7 – 2.790
R² = 0.786
16
0
AN_P1 (mm²)
1
0
AN_P2..7 (mm²)
6620
76
AN_S1 (mm²)
1
0
AN_S2..7 (mm²)
Soils
1A, 1C – PZ-ab
2A, 2C – AR-br.dy
3A, 3Ck – CH-ha
4A, 4Ck – CM-eu
CMP classes
1 0–0.200
2 0.201–0.400
3 0.401–0.600
4 0.601–0.800
5 0.801–1.000
6 1.001–1.200
7 >1.200

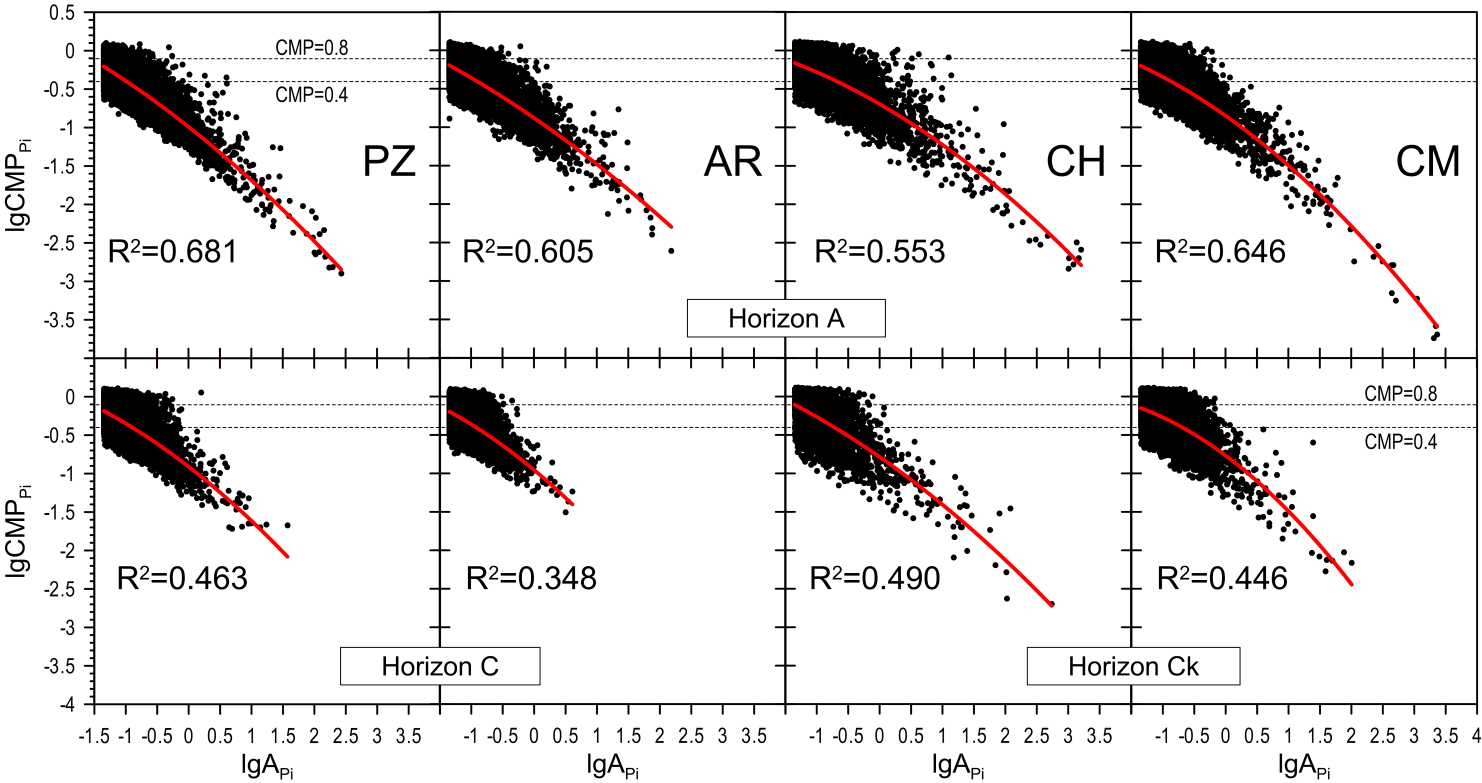
lgCMP_Pi
lgA_Pi
CMP=0.8
CMP=0.4
PZ
AR
CH
CM
R²=0.681
R²=0.605
R²=0.553
R²=0.646
Horizon A
R²=0.463
R²=0.348
R²=0.490
R²=0.446
Horizon C
Horizon Ck

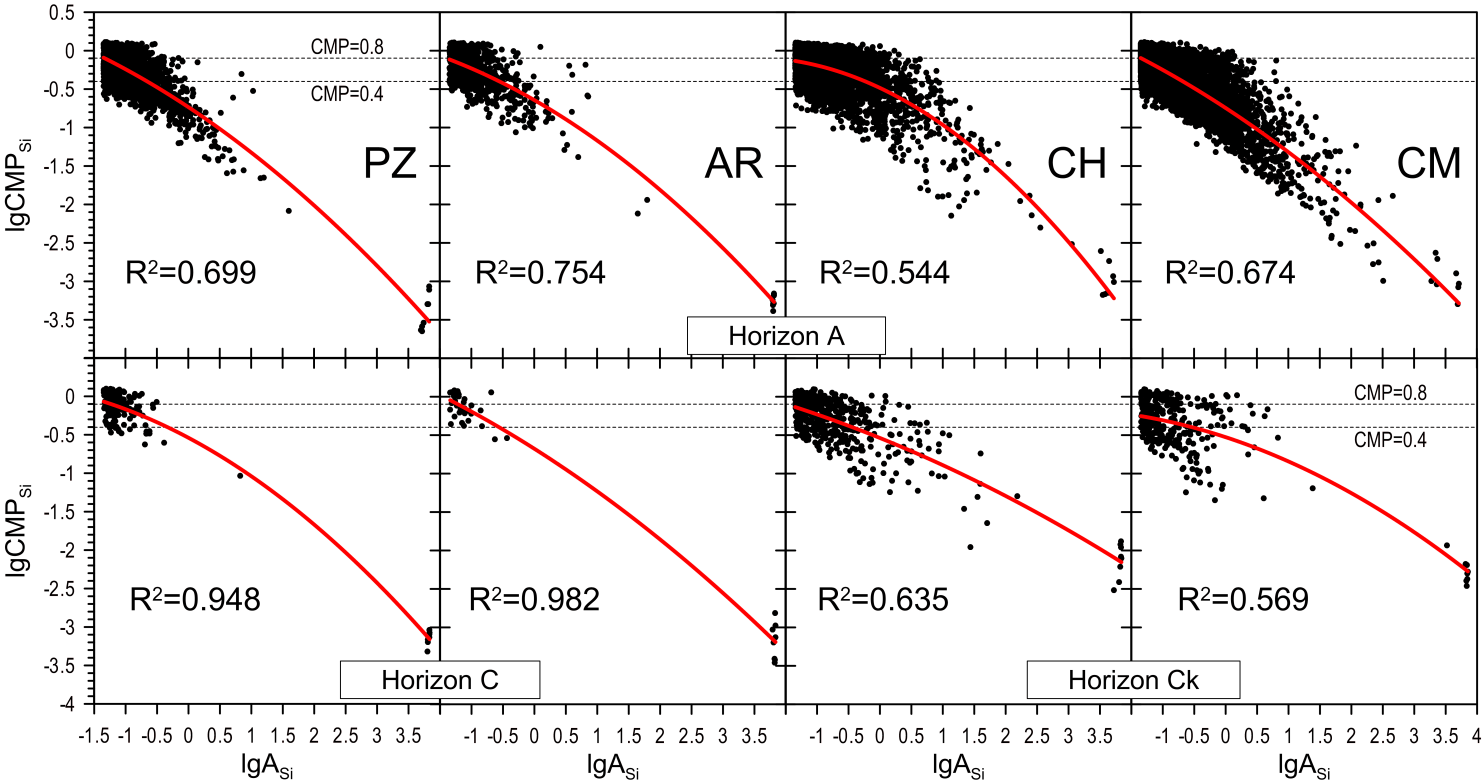
lgCMP$_{Si}$
lgA$_{Si}$
CMP=0.8
CMP=0.4
PZ
AR
CH
CM
R^2=0.699
R^2=0.754
R^2=0.544
R^2=0.674
Horizon A
R^2=0.948
R^2=0.982
R^2=0.635
R^2=0.569
Horizon C
Horizon Ck